

THE GOULD BELT ‘MISFITS’ SURVEY: THE REAL SOLAR NEIGHBORHOOD PROTOSTARS

AMANDA HEIDERMAN^{1,2,3,4} AND NEAL J. EVANS II⁵*Draft version July 6, 2021*

ABSTRACT

We present an HCO⁺ $J = 3 \rightarrow 2$ survey of Class 0+I and Flat SED young stellar objects (YSOs) found in the Gould Belt clouds by surveys with *Spitzer*. Our goal is to provide a uniform Stage 0+I source indicator for these embedded protostar candidates. We made single point HCO⁺ $J = 3 \rightarrow 2$ measurements toward the source positions at the CSO and APEX of 546 YSOs (89% of the Class 0+I + Flat SED sample). Using the criteria from van Kempen et al. (2009), we classify sources as Stage 0+I or bona fide protostars and find that 84% of detected sources meet the criteria. We recommend a timescale for the evolution of Stage 0+I (embedded protostars) of 0.54 Myr. We find significant correlations of HCO⁺ integrated intensity with α and T_{bol} but not with L_{bol} . The detection fraction increases smoothly as a function of α and L_{bol} , while decreasing smoothly with T_{bol} . Using the Stage 0+I sources tightens the relation between protostars and high extinction regions of the cloud; 89% of Stage I sources lie in regions with $A_V > 8$ mag. Class 0+I and Flat SED YSOs that are not detected in HCO⁺ have, on average, a factor of ~ 2 higher T_{bol} and a factor of ~ 5 lower L_{bol} than YSOs with HCO⁺ detections. We find less YSO contamination, defined as the number of undetected YSOs divided by the total number surveyed, for sources with $T_{bol} \lesssim 600$ K and $L_{bol} \gtrsim 1 L_\odot$. The contamination percentage is $> 90\%$ at $A_V < 4$ mag and decreases as A_V increases.

Subject headings: ISM: clouds; dust; extinction; galaxies: ISM; galaxies: star formation; infrared: stars; stars: formation

1. INTRODUCTION

The evolution of dense molecular cores into stars has been characterized by observational changes in their spectral energy distributions (SEDs) since the seminal suggestions by Lada & Wilking (1984) and Adams et al. (1987). In this picture the changes in the SED, captured either by the spectral index from 2 to 25 μm in the original Class system, or the bolometric temperature (Chen et al. 1995), track the movement of matter from core to disk to star. Adams et al. (1987) connected the observational measures of the SED (Classes) to physical configurations (Stages). The stage referred to as I in the original work included all the time that the forming star was surrounded by an envelope, a phase also referred to as a protostar, or the embedded phase.

Andre et al. (1993) sub-divided Stage I into 0 and I, with Stage 0 sources having more mass in the envelope than in the star plus disk. Stage I sources had more mass in the star plus disk than in the envelope, but still some envelope material. We have no way to distinguish these, so we lump these together in this paper, referring to them as Stage 0+I. Thus, a Stage 0+I source consists of a star and disk embedded in a dense, infalling envelope, while a Stage II source contains only a star and disk.

The exact relationship between observations and physical configuration required further definition.

Robitaille et al. (2006) suggested defining Stage 0+I sources as those with substantial mass infall rates (\dot{M}_{inf}) compared to stellar masses (M_\star), requiring $\dot{M}_{inf}/M_\star > 10^{-6} \text{ yr}^{-1}$. However, these two quantities are difficult to determine from observations, and \dot{M}_{inf} is not related monotonically to evolutionary Stage in models of episodic accretion (Dunham et al. 2010; Dunham & Vorobyov 2012). Crapsi et al. (2008) found that the usual evolutionary tracers, like the spectral index in the near-infrared to mid-infrared or the bolometric temperature (T_{bol}) could be misleading for sources with large inclination angles, but that $0.2 M_\odot$ in the envelope was a reasonable indicator to select Stage 0+I sources.

van Kempen et al. (2009) showed that detection of the HCO⁺ $J = 4 \rightarrow 3$ line was a good indicator of a Stage 0+I source. In particular they suggested that an integrated intensity, $I_{MB} \equiv \int T_{MB} dV$, of 0.4 K km s^{-1} is a good metric for a Stage 0+I source, because lower values of integrated intensity could arise if only a disk were present. To further discriminate against disk emission and unrelated emission from sources nearby in the sky, they also suggested that the HCO⁺ emission should be extended, but peaked on the source, or that submillimeter dust continuum emission be extended but peaked on the source.

The c2d (Evans et al. 2009) and Gould Belt (Dunham, in prep.) projects together surveyed essentially all nearby ($d < 500 \text{ pc}$) molecular clouds, except for Taurus and Orion. They used a common classification scheme for YSOs based on the spectral index between 2 and 24 μm , using whatever photometry was available between those wavelengths. The spectral index is defined by

$$\alpha = \frac{d \log(\lambda S(\lambda))}{d \log(\lambda)}, \quad (1)$$

¹ Department of Astronomy, University of Virginia, P.O. Box 400325, Charlottesville, VA 22904, USA; heiderman@virginia.edu

² National Radio Astronomy Observatory, 520 Edgemont Road, Charlottesville, VA 22903, USA

³ Max-Planck-Institut für Astronomie, Königstuhl 17, D-69117 Heidelberg, Germany

⁴ NSF Astronomy and Astrophysics Postdoctoral Fellow

⁵ Department of Astronomy, The University of Texas at Austin, 2515 Speedway, Stop C1400, Austin, Texas 78712-1205, USA; nje@astro.as.utexas.edu

where $S(\lambda)$ is the spectral flux density at wavelength λ .

Building on work by Greene et al. (1994), Evans et al. (2009) defined the divisions between classes as follows:

0+I $0.3 \leq \alpha$;

Flat SED $-0.3 \leq \alpha < 0.3$;

II $-1.6 \leq \alpha < -0.3$;

III $\alpha < -1.6$.

The Class 0+I sources are widely associated with Stage 0+I, while Class II sources are associated with Stage II (star and disk dominated objects), but the status of Flat SED sources has been unclear.

When using α alone, there is no distinction between Class 0 and Class I sources, so both are included when we use Class 0+I, and Stage 0+I encompasses the entire phase with a star/disk and surrounding envelope with $M > 0.2 M_{\odot}$.

Our goal is to provide a uniform indicator of whether Class 0+I and Flat SED sources in the survey of the Gould Belt clouds are likely to be Stage 0+I sources. Because there were over 500 Class 0+I and Flat SED sources in the original sample, mapping of each source was impractical, so we made single point measurements toward the positions of each YSO instead. We also used the $J = 3 \rightarrow 2$ transition of HCO^+ , as the atmospheric conditions required are less stringent than for the $J = 4 \rightarrow 3$ line. We describe here the results of the MISidentified YSOs from SED FITS (MISFITS) Survey.

2. OBSERVATIONS AND SPECTRAL REDUCTION

Observations of the HCO^+ $J = 3 \rightarrow 2$ transition were obtained with the heterodyne receiver at the Caltech Submillimeter Observatory⁶ during runs in 2009 (June and December), 2010 (July and December), 2011 (July), and 2012 (June and September). The main beam efficiencies (η_{MB}) were determined on each run by observations of planets. The characteristics of the equipment are indicated in Table 1, including the pointing uncertainties and the main beam efficiency. The pointing uncertainties are the standard deviation of all pointing measurements through the run. Since the pointing offsets were continually corrected, the actual pointing errors on a given source are less than the values in the table. The values of η_{MB} were determined by observations of planets, generally Jupiter or Saturn. They were relatively constant over the various runs with $\langle \eta_{\text{MB}} \rangle = 0.67 \pm 0.03$, except for the 2012 June run, when suitable planetary calibrators were not available. We have used $\eta_{\text{MB}} = 0.67$ for all runs, including the 2012, June run.

The most southerly clouds, Musca and Chamaeleon, were observed with the APEX⁷ telescope in 2011, October. The APEX-1 receiver and the XFFTS spectrometer were used to obtain a spectral resolution of about 0.085 km s^{-1} . The forward efficiency of the telescope is 0.95

⁶ The Caltech Submillimeter Observatory was operated by the California Institute of Technology, until 2013 April 1 under cooperative agreement with the National Science Foundation (AST-0838261)

⁷ APEX is a collaboration between the Max-Planck-Institut für Radioastronomie, the European Southern Observatory, and the Onsala Space Observatory.

Table 1
Observing Parameters

Run	Pointing Uncertainty (arcsec)	Efficiency
(1)	(2)	(3)
2009 June	5''9	0.67
2009 December	6''7	0.63
2010 July	6''7	0.67
2010 December	4''9	0.64
2011 July	7''8	0.66
2011 December	8''0	0.71
2012 June	10''2	0.67 ^a
2012 September	7''6	0.69

^a Value set to the mean of all other observing runs because no suitable calibrator was available.

and the beam efficiency is 0.75 (values taken from the APEX website) corresponding to $\eta_{\text{MB}} = 0.75/0.95 = 0.79$. Weather conditions were variable, so integration time was adjusted to achieve an rms noise of 0.08 K.

The standard data reduction process consisted of averaging multiple observations when relevant, box-car averaging to an effective spectral resolution of 0.2 km s^{-1} for CSO data, 0.17 km s^{-1} for APEX data, fitting a baseline (usually first-order, but occasionally higher order), and fitting a Gaussian if a line was evident. Because the main goal was to find out if a detectable line was present, the fitting process was generally not carefully tuned for optimum parameter estimation. In several clouds, multiple velocity components were present; these were sometimes separable and sometimes too blended to resolve. When separable, two Gaussians were fitted and both results are given (see Table 5 in Appendix).

When no line was convincingly detected, an upper limit was obtained by calculating the integrated intensity over a velocity range where lines were detected in that cloud and the uncertainty in that value. The upper limit was taken to be the absolute value of the area plus twice the uncertainty. Some of the higher upper limits reflect emission that was systematically high over the range of relevant velocities but did not produce a convincing line profile.

3. RESULTS

For this survey, we compare observations to the table of YSOs from the work of Dunham et al. (2013). The full list of sources with HCO^+ observations is given in Table 5 in the Appendix. The HCO^+ observations were obtained at positions of sources identified in earlier versions of the catalogs. Some of these sources are no longer accepted as YSOs, a few other sources have been added, and there are some positional discrepancies. To match observations with sources in the latest catalogs, we searched for HCO^+ observations within $14''$ (half the CSO beam) of the source. However, only 4 sources lie more than $6''$ from the pointing position, with the vast majority still exactly at the pointing center. In a few cases, more than one observation was found within $14''$. The line measurements were similar, so we used the observations from the nearest position to the infrared source. In addition, some sources have changed classifications since the original catalog was made, and we use the new classifications. As a result, we have some sources that are now

classified as Class II according to the spectral index. We include results on these, but we caution that they are not representative of most Class II sources because they are relatively close to the boundary between Class II and Flat sources. Figure 4 shows the distribution of spectral index for the observed sample and for the full catalog of YSOs. Our observed sample becomes very incomplete for $\alpha < -0.3$.

The results of the observations are listed in Table 5 in the Appendix. The summary of results by cloud is in Table 4. For each cloud with sufficient detections, a composite spectrum was constructed from all the detected sources. From these average spectra, a characteristic velocity and linewidth were added to Table 4. When two velocity components could be separated in the composite spectrum, values are given for each.

4. ANALYSIS

Taking all clouds into account, there are 326 Class 0+I sources, 209 Flat SED sources, and 1243 Class II sources in the tables of YSOs from the work of Dunham et al. (2013). Because our survey was based on earlier catalogs (§3), our coverage is slightly incomplete. We observed 288 Class 0+I sources (88% of the full sample), 188 Flat SED sources (90% of the full sample), and 70 Class II sources (6% of the full sample). Our statistics will be based on that subsample.

4.1. Results Based on Any Detection

For a first estimate, we consider all detections, regardless of strength, within the sample of observed sources. For that criterion and sample, 240 (83%) of Class 0+I YSOs have detections, while 112 (60%) of Flat SED sources have detections, and 28 (40%) of Class II sources have detections. To estimate the number of Stage 0+I sources based on detection of the line, we could add the Flat SED and Class II sources that are detected to the list of Stage 0+I sources, yielding a number of 380 potential Stage 0+I sources out of 546 observed sources.

If we assume that our sample of observed sources was not biased, we can use the detection percentages to extrapolate to the number that would be detected in the full catalog. This analysis yields numbers of plausible detected sources of 271 Class 0+I sources and 125 Flat SED sources for a total of 396 likely detected sources within those two classes (Table 3). We do not include the Class II sources in the extrapolated statistics because the Class II sample was clearly biased.

In contrast, the selection of Class 0+I and Flat SED sources was not biased by the values of α , strength of infrared emission, or any other variable known to us. The quite small fraction of sources that remained unobserved resulted entirely from time limitations.

These numbers are certainly an overestimate for the following reasons.

1. Some sources without their own dense envelopes may be superimposed on emission from dense envelopes of other sources. This possibility can be examined only with mapping and detailed analysis, which was not possible for this large sample. The study by Carney et al. (in prep.) with mapping of a smaller sample will allow some estimates of the size of this effect.

2. Weak lines may be associated with very low mass remnant envelopes or even disks. While a quantitative relation between HCO^+ emission and mass has not been established, we will follow the example of van Kempen et al. (2009), who set a minimum value for the integrated intensity (§4.2). This threshold was intended to eliminate Stage II sources (disk-only), which may have HCO^+ emission.

4.2. Results for a Threshold Emission Strength

van Kempen et al. (2009) applied a series of requirements to decide if sources were in Stage 0+I. The main requirement was that the HCO^+ was extended, but peaked on the source with an integrated intensity, $I_{\text{MB}} > 0.4 \text{ K km s}^{-1}$. If the HCO^+ was not extended, an alternative criterion required continuum emission from dust at $850 \mu\text{m}$ to be extended, but peaked on the source. Because we do not have maps, the only criterion we can easily apply is one on the strength of the $\text{HCO}^+ J = 3 \rightarrow 2$ emission. The criterion used by van Kempen et al. (2009) was that $I_{\text{MB}} > 0.4 \text{ K km s}^{-1}$, for the $J = 4 \rightarrow 3$ line. To translate this limit to our slightly more easily excited line, we compared values of I_{MB} for our $J = 3 \rightarrow 2$ lines with a sample of 27 sources also observed in the $J = 4 \rightarrow 3$ line by Carney et al. (in prep.). The $J = 4 \rightarrow 3$ maps were convolved to the $28''$ beam size of the CSO single pointing observations and the spectra were fitted using a single line Gaussian profile. For that sample our values of I_{MB} are 1.70 ± 0.10 times higher, where the uncertainty is the standard deviation of the mean. Therefore, the equivalent I_{MB} for the $J = 3 \rightarrow 2$ line to the van Kempen et al. (2009) criterion is $I_{\text{MB}} \geq 0.68 \text{ K km s}^{-1}$. We have also compared our sample to the Ophiuchus sample observed by van Kempen et al. (2009) and found 17 sources with detections that overlap in both samples. If we include these sources in our average line ratio, we find that our $J = 3 \rightarrow 2$ line measurements are 1.58 ± 0.10 times higher than the $J = 4 \rightarrow 3$ integrated intensities. We note that these maps are at a higher resolution and are not convolved to the same beam size of our measurements. With this caveat in mind, we will use the $I_{\text{MB}} \geq 0.68 \text{ K km s}^{-1}$ criteria for the threshold in our analysis, but note in the following paragraph the differences. As noted above, the threshold was intended to discriminate against HCO^+ emission from disks; disk emission would be highly diluted in our beam, so our scaled up threshold is a conservative choice that probably excludes some Stage 0+I sources with low-mass envelopes.

What changes if we apply a cut to the integrated intensity so that only sources with a value above that threshold would qualify as Stage 0+I sources? With this criterion, there are 208/288 (72%) and 90/188 (48%) of the observed Class 0+I sources and Flat SED sources with I_{MB} above that threshold, respectively. The status of Flat SED sources has never been very clear, but they have been assumed to be a transitional class. The fact that roughly half achieve Stage 0+I status by the standards we are using is consistent with that picture. Interestingly, 21 Class II sources (30% of the observed sources) also satisfy that criterion. If we instead used the slightly lower I_{MB} threshold average of 0.63 K km s^{-1} from both the Carney et al. (in prep.) and van Kempen et al.

(2009) samples, we find 13 additional sources above the threshold or 213/288 (74%) of Class 0+I, 95/188 (51%) Flat SED, and 24 Class II sources. The detected Class II sources have values of α that are highly skewed toward the boundary between Class II and Flat SEDs. Since these were originally classified as either Class 0+I or Flat (to be included in our sample), they could be Stage 0+I sources with envelopes that are less opaque or that are viewed closer to face-on. They could also be caused primarily by contamination (projected on HCO^+ emission from another source or extended emission); comparison to detections of submillimeter continuum emission (see §4.3) suggest the latter explanation.

The number of sources detected above threshold is listed for each cloud in column 12 of Table 4. As in §4.1, we extrapolate to the full sample for Class 0+I and Flat SED sources, but not for Class II sources. These results are summarized in Table 3.

4.3. Comparison to Far-Infrared or Submillimeter Continuum Emission Detections

Detection of submillimeter continuum emission concentrated on an infrared source, but extended more than would be expected of a disk, is another criterion often used to identify Stage 0+I sources (e.g. van Kempen et al. 2009). We do not have a complete survey of our sample for submillimeter continuum emission, but we can compare to the 167 sources with submillimeter observations within our sample, as tabulated by Dunham et al. (2013). Table 2 gives the numbers for various combinations of detections above threshold of HCO^+ and a far-infrared or submillimeter continuum emission detection in a wavelength range $70\mu\text{m} < \lambda < 850\mu\text{m}$.

Of the sources in our sample with submillimeter detections, 91 of those are detected in HCO^+ and 4 are undetected, 85 above the threshold of 0.68 K km s^{-1} . Only 4 sources with submillimeter emission have no HCO^+ detection and 6 have a weak detection ($I_{\text{MB}} < 0.68 \text{ K km s}^{-1}$). There is thus generally strong agreement between the HCO^+ and submillimeter criteria. There are however, 55 sources with strong HCO^+ detections and submillimeter data, but no submillimeter detection. Without more information on the sensitivity of the submillimeter data, it is hard to decide if there is real disagreement.

Very few sources with submillimeter continuum detections are undetected in HCO^+ . Since the sample with submillimeter detections is different, there are 35 sources with submillimeter detections that we did not observe. If one added all the sources with submillimeter detections to the list of Stage 0+I candidates, the numbers and timescales would increase, but not substantially.

We can also examine the changes in the agreement between HCO^+ and submillimeter continuum emission with respect to SED class. There are 52 Class 0+I and Flat SED sources that meet the Stage 0+I emission criteria but do not have submillimeter emission and 162 sources that have not been observed in the submillimeter. There is only 1 submillimeter detection out of the 21 Class II sources that meet the HCO^+ Stage 0+I criteria. That fact clearly suggests that HCO^+ detections toward Class II sources are likely to be due to contamination. We include all the numbers so that readers can make their own judgments, but we favor the values in Table

3 that are extrapolated to the full sample but without Class II sources.

4.4. Timescales for Stage 0+I

The standard calculation for how long is spent in a given class uses the number of sources in that class, the number of sources in a reference class, and an assumed timescale for that reference class (e.g., Evans et al. 2009). The reference class has generally been taken to be Class II objects. While some Class II sources do have HCO^+ emission, it may be caused by confusion. In the absence of maps that could test that possibility, we will continue to associate Class II sources with Stage II sources, those without substantial envelopes but with infrared excess indicative of a disk. Therefore we will calculate the duration of the Stage 0+I phase using the following equation.

$$\Delta t(\text{Stage 0+I}) = \Delta t(\text{Class II}) \frac{N(\text{Stage 0+I})}{N(\text{Class II})} \quad (2)$$

Table 3 shows the numbers of sources and associated timescales for various possible calculations. The timescales in this table assume a Class II duration of 2 Myr for consistency with previous work (but see below). We show results for any detection and for detections above the threshold, $I_{\text{MB}} \geq 0.68 \text{ K km s}^{-1}$. The numbers indicated by “Raw” count only actual detections but include any class. The numbers indicated by “Extrapolated” account for the incomplete sampling of the full catalog, using the fraction observed, but only in Class 0+I and Flat SED, because the Class II sample was highly incomplete and very biased.

With 1243 Class II YSOs in the clouds, the estimates in Table 3 for $\Delta t(\text{Stage 0+I})$ range from 0.51 to 0.62 Myr. As discussed above, we recommend the value based on extrapolation to the full sample, but excluding Class II sources; in this case the timescale for Stage 0+I is 0.54 Myr for a Class II timescale of 2 Myr. This timescale is very similar to that found for Class 0+I sources alone by Evans et al. (2009) for the c2d clouds and slightly larger than timescales found for Class 0+I sources in the Taurus and Orion clouds when similar criteria were used (Dunham et al. 2014). The loss of some Class 0+I objects has been compensated by the addition of some Flat SED objects, but now we have a better estimate for the timescale of the entire embedded phase.

As noted above, in previous analyses, we have assumed that the fraction of YSOs with infrared excess declines exponentially with a half-life of $2 \pm 1 \text{ Myr}$ (Mamaejek 2009). However, these estimates depend entirely on the timescales for loss of infrared excess. Recently, longer timescales have been suggested by studies of older associations (Soderblom et al. 2014), and models of disk evolution suggest a relatively constant and high fraction of disks up to about 2.5 Myr, followed by a rapid decrease from 2.5 to 4 Myr (Alexander & Armitage 2009). Observations accounting for more rapid dissipation of disks around close binaries are broadly consistent with this model (Kraus et al. 2012). Consequently, the timescales for Stage 0+I could easily be 1.5-2 times longer.

Conversely, the timescales could be shorter if we added in the denominator in equation 2 the Class III sources with infrared excesses as seen by *Spitzer* surveys. If these

are also counted in the statistics of infrared excess in clusters, then the half-life from cluster studies includes that fraction of Class III objects. Early studies of disk fraction in clusters were less sensitive to small excesses than was *Spitzer*, but recent studies by Ribas et al. (2014), using *Spitzer* data on 22 associations, provide the most comparable sample. They find that the timescale for infrared excess depends on the wavelength where the excess first appears and on stellar mass (Ribas et al. 2015). The timescales in the last reference, converted from $1/e$ time to half-life, range from 1.9 to 3.0 Myr, with the larger time corresponding to excesses beginning at wavelengths as long as 20 μm . The latter is probably the best value for comparison if we include our Class III sources. There are 1188 Class III objects in the tables of YSOs from Dunham et al. (2013). Some infrared excess at wavelengths out to 24 μm was required for these to become YSO candidates. If we include those in equation 2 and take a 3.0 Myr half-life, the timescale for Stage 0+I drops to 0.41 Myr. We note, however, that our class III sample may be ~ 50 – 100% contaminated by background asymptotic giant branch (AGB) stars (Dunham et al., in prep.). For example, if the number of class III sources had at least 50% AGB star contamination, we would still obtain a similar Stage 0+I timescale of 0.55 Myr.

4.5. Correlations

In this section, we consider how I_{MB} correlates with various quantities used to trace evolution. If α decreases and T_{bol} increases as the envelope mass decreases, one might expect correlations (positive and negative respectively) of the HCO^+ emission with these quantities. However, the emission from HCO^+ is not simply proportional to the mass of the envelope. Warmer and denser gas will emit more strongly. We have no direct measure of those quantities, but the gas temperature will be higher around sources of higher luminosity.

Figure 5 plots I_{MB} versus the spectral index, α , T_{bol} , and L_{bol} , with inverted triangles indicating upper limits. In cases where lines had two velocity components, we used the I_{MB} of the stronger line. The grey solid lines show the α values that separate the SED classes.

In the I_{MB} versus T_{bol} plot, we can separate Class 0 from Class I, and we also show the divisions between classes for extinction-corrected T_{bol} suggested by Evans et al. (2009):

0 $T_{\text{bol}} < 70 \text{ K}$;

I $70 \text{ K} \leq T_{\text{bol}} \leq 500 \text{ K}$;

Flat $500 \text{ K} < T_{\text{bol}} \leq 1450 \text{ K}$;

II $1450 \text{ K} < T_{\text{bol}} \leq 2800 \text{ K}$.

The data are very scattered, but there are trends for stronger emission with larger α (left panel), smaller T_{bol} , and possibly larger L_{bol} . To test for a significant (3σ) correlation, we require the absolute values of the Pearson correlation coefficient to exceed $3/\sqrt{N-1}$, where N is the number of data points. Including all detections, we have 377 data points (3 have no values for α), so we test for $|r| > 0.16$. The tests are done for $\log I_{\text{MB}}$ versus α , $\log T_{\text{bol}}$, and $\log L_{\text{bol}}$. We find significant correlation for α ($r = 0.26$), and an anti-correlation for T_{bol}

($r = -0.26$), but not for L_{bol} ($r = 0.15$). The fraction of sources with detections above the threshold shows a strong and smooth correlation with evolutionary indicators. Figure 6 shows the detection fraction of all sources above the I_{MB} threshold for Stage 0+I sources in bins of α , $\log T_{\text{bol}}$, and $\log L_{\text{bol}}$. The detection fraction increases strongly with α through the flat category and is 80% or greater for sources with $\alpha > 0.75$. The fraction with detections steadily increases as T_{bol} decreases or L_{bol} increases.

4.6. The Distribution of Stage 0+I Sources

Based on preliminary results of this survey for HCO^+ , Heiderman et al. (2010) showed that Class 0+I and Flat SED sources were strongly concentrated into regions with large-scale extinction above 7 or 8 mag, and that this statement became stronger when sources without HCO^+ emission (MISFITS) were removed. We can now revisit this result with the full sample. Figure 7 shows the A_V at the source position, determined from background star extinctions averaged over $270''$, for both Stage 0+I and all 535 Class 0+I and Flat SED YSOs in the sample. The sample of all Class 0+I and Flat SED sources (dotted histogram) are concentrated toward regions of high extinction, with 75% of all Class 0+I and Flat SED sources found toward $A_V > 8 \text{ mag}$ (black vertical dashed line). Stage 0+I sources (black hashed histogram) are still more strongly concentrated in regions of high extinction with 89% of them above $A_V = 8 \text{ mag}$ and the MISFITS (red hashed histogram) are distributed evenly on either side of $A_V = 8 \text{ mag}$ line. Figure 8 shows the distribution of bona fide Stage 0+I protostars and MISFITS in the Perseus molecular cloud. The background image is the extinction map with a $180''$ resolution and contours ranging from 2 to 41 in intervals of 4 mag. The black contour outlines the extinction map at the completeness limit of $A_V = 2 \text{ mag}$ and the green contour shows where $A_V = 8 \text{ mag}$. The yellow stars are Stage 0+I protostars. Sources that are filled cyan circles with an open star correspond to MISFITS that are undetected in $\text{HCO}^+ J = 3 \rightarrow 2$ emission.

It is important to recall that the extinction maps are based on star counting and have much poorer spatial resolution than the HCO^+ observations. High extinction is not just a reflection of the local core density. In fact, one might expect some MISFITS at high extinction, which would distort the mid-infrared SED, despite our efforts to correct for it. Indeed there are a few such objects in the histogram, but the main trend is for a higher HCO^+ detection fraction in regions of higher large-scale extinction.

4.7. Properties of the MISFITS

We can explore trends in properties of the MISFITS or YSOs undetected in $\text{HCO}^+ J = 3 \rightarrow 2$. In Figure 9, we compare the number of MISFITS (black hashed histogram) to Class 0+I and Flat SED YSOs that are detected in HCO^+ , and Stage 0+I protostars with strong HCO^+ emission versus T_{bol} and L_{bol} . In all cases, the distributions for Stage 0+I sources are skewed with respect to those of the MISFITS. The median values for T_{bol} and L_{bol} are 353 K and $0.43 L_\odot$ for Stage 0+I sources (detected above threshold), 774 K and $0.083 L_\odot$ for MISFITS, and 330 K and $0.41 L_\odot$ for YSOs detected at any

Table 2
Stage 0+I Sources vs. Submm detections

Criteria (1)	Number (2)
Strong line detection ^a	319
Strong line detection + Submm detection	85
Strong line detection or Submm detection	329
Strong line detection + Submm undetected	55
Weak line detection + Submm detection	6
HCO ⁺ Undetected + Submm detection	4
Source not in HCO ⁺ survey + Submm detection	35

^a Strong line defined as a source meets the $I_{\text{MB}} > 0.68$ K km s⁻¹ detection criteria.

Table 3
Numbers and Timescales for Stage 0+I Sources

Quantity 1	Sample 2	Detected 3	$I_{\text{MB}} > 0.68$ K km s ⁻¹ 4	Include Class II? 5
Number	Raw	380	319	Yes
Number	Extrapolated	396	335	No
Timescale	Raw	0.62 Myr	0.51 Myr	Yes
Timescale	Extrapolated	0.64 Myr	0.54 Myr	No

level, respectively. In general, Class 0+I and Flat SED YSOs that are undetected in HCO⁺ have a factor of ~ 2 higher T_{bol} and a factor of ~ 5 lower L_{bol} than detected YSOs.

Figure 10 shows L_{bol} versus T_{bol} for all YSOs observed in HCO⁺ separated by Class as determined from α (Class 0+I, Flat SED, and Class II are diamonds, squares, and circle solid points, respectively). Undetected YSOs or MISFITS are shown in color (Class 0+I, Flat SED, and Class III are red, green, and blue solid points, respectively) with an open star. Stage 0+I protostars are indicated by the yellow stars. The percent of YSO contamination defined as the number of MISFITS divided by the total surveyed in a bin is shown color coded from more (red) to less (yellow). Low ($< 17\%$) contamination is found where $T_{\text{bol}} \lesssim 600$ K and $L_{\text{bol}} \gtrsim 1 L_{\odot}$. We further explore the percent of YSO contamination versus A_V in Figure 11. The contamination fraction is $> 90\%$ at $A_V < 4$ mag and decreases with increasing A_V . The rise above $A_V = 20$ mag is due to low number statistics.

5. SUMMARY

The goal of this work was to identify Stage 0+I sources (those with a substantial envelope of dense gas) among the larger sample of Class 0+I and Flat SED sources. To achieve this, we have surveyed for emission in the $J = 3 \rightarrow 2$ line of HCO⁺ toward 546 sources in nearby clouds. The sample is based on the YSO lists for the combined c2d and Gould Belt surveys with Spitzer. It is focused on Class 0+I and Flat SED sources, but a few Class II sources were included. The surveyed sources represent 88% of the Class 0+I sources and 90% of the Flat SED sources in the full list of YSOs in Dunham et al. (2013).

If we apply a threshold integrated intensity of $I_{\text{MB}} \geq$

0.68 K km s⁻¹ to define a Stage 0+I source, 72% of the Class 0+I and 48% of the Flat SED sources would be classified as Stage 0+I sources (§ 4.2). A few Class II sources were also detected, but these sources were originally classified as Flat or Class 0+I sources, so are very unrepresentative of the much larger group of Class II sources. If we exclude them, but extrapolate (modestly) to the full c2d plus Gould Belt sample, we predict 335 Stage 0+I sources in all the clouds.

Based on a 2 Myr timescale for Class II sources, the most appropriate timescale for Stage 0+I (the entire embedded phase) would be 0.54 Myr (§ 4.4 and Table 3). Other choices for how to calculate this number are certainly possible, and we have tried to supply enough information so that other calculations could be made.

There is a good, but imperfect, agreement between HCO⁺ detections and far-infrared or submillimeter continuum emission (§ 4.3), within the limited sample with both kinds of data available.

The HCO⁺ detection fraction increases with spectral index (α) and bolometric luminosity (L_{bol}), and decreases with bolometric temperature (T_{bol}), all trends that one might expect (§ 4.5). In particular, nothing distinctive occurs within the Flat SED category, and about half of those sources qualify as Stage 0+I sources, suggesting that this category has no physical significance. Unlike the rather smooth dependence of the detection fraction on the usual evolutionary indicators, the *strength* of the HCO⁺ emission scatters widely but trends versus these possible evolutionary indicators are clearly significant. Other variables clearly affect the HCO⁺ emission strength, but the correlation of emission strength with L_{bol} is not significant.

The concentration of Class 0+I and Flat SED sources to regions of high extinction seen in our previous study (Heiderman et al. 2010) is strengthened when consideration is narrowed to Stage 0+I sources (§ 4.6).

YSOs undetected in HCO⁺ lie preferentially at higher T_{bol} and at lower L_{bol} than detected YSOs. The YSO contamination, defined as the number of undetected YSOs divided by the total surveyed, is low where $T_{\text{bol}} \lesssim 600$ K and $L_{\text{bol}} \gtrsim 1 L_{\odot}$. The contamination fraction is $> 90\%$ at $A_V < 4$ mag and decreases with increasing A_V .

We thank M. Dunham, J-H. Chen, H-J. Kim, J. Green, C. Salyk, M. Merello, N. Vutisalchavakul, I. Oliveira, M. Song, and E. Yu for assistance in obtaining observations at the CSO and A. Gusdorf, G. Siringo, and J. Forbrich for assistance at APEX. We also thank M. Carney and E. van Dishoeck for providing their HCO⁺ $J = 4 \rightarrow 3$ data for comparison in advance of publication and T. Huard for informative discussions. ALH is supported by an NSF AARP under award AST-1302978. NJE is supported by NSF Grant AST-1109116 to the University of Texas at Austin. NJE thanks the European Southern Observatory, Santiago, for hospitality during an extended visit when some of this work was done. This work was partially carried out in the Max-Planck Research Group *Star formation throughout the Milky Way Galaxy* at the Max-Planck-Institut für Astronomie.

REFERENCES

- Adams, F. C., Lada, C. J., & Shu, F. H. 1987, *ApJ*, 312, 788
- Alcalá, J. M., Spezzi, L., Chapman, N., et al. 2008, *ApJ*, 676, 427
- Alexander, R. D. & Armitage, P. J. 2009, *ApJ*, 704, 989
- Andre, P., Ward-Thompson, D., & Barsony, M. 1993, *ApJ*, 406, 122
- Bontemps, S., André, P., Könyves, V., et al. 2010, *A&A*, 518, L85
- Broekhoven-Fiene, H., Matthews, B. C., Harvey, P. M., et al. 2014, *ApJ*, 786, 37
- Chen, H., Myers, P. C., Ladd, E. F., & Wood, D. O. S. 1995, *ApJ*, 445, 377
- Comerón, F. 2008, *The Lupus Clouds*, ed. B. Reipurth, 295
- Crapsi, A., van Dishoeck, E. F., Hogerheijde, M. R., Pontoppidan, K. M., & Dullemond, C. P. 2008, *A&A*, 486, 245
- Dunham, M. M., Arce, H. G., Allen, L. E., et al. 2013, *AJ*, 145, 94
- Dunham, M. M., Evans, II, N. J., Terebey, S., Dullemond, C. P., & Young, C. H. 2010, *ApJ*, 710, 470
- Dunham, M. M., Stutz, A. M., Allen, L. E., et al. 2014, *Protostars and Planets VI*, 195
- Dunham, M. M. & Vorobyov, E. I. 2012, *ApJ*, 747, 52
- Evans, II, N. J., Dunham, M. M., Jørgensen, J. K., et al. 2009, *ApJS*, 181, 321
- Greene, T. P., Wilking, B. A., Andre, P., Young, E. T., & Lada, C. J. 1994, *ApJ*, 434, 614
- Gutermuth, R. A., Bourke, T. L., Allen, L. E., et al. 2008, *ApJ*, 673, L151
- Harvey, P. M., Fallscheer, C., Ginsburg, A., et al. 2013, *ApJ*, 764, 133
- Harvey, P. M., Huard, T. L., Jørgensen, J. K., et al. 2008, *ApJ*, 680, 495
- Heiderman, A., Evans, II, N. J., Allen, L. E., Huard, T., & Heyer, M. 2010, *ApJ*, 723, 1019
- Kirk, J. M., Ward-Thompson, D., Di Francesco, J., et al. 2009, *ApJS*, 185, 198
- Lada, C. J. & Wilking, B. A. 1984, *ApJ*, 287, 610
- Lee, J.-E., Di Francesco, J., Bourke, T. L., Evans, II, N. J., & Wu, J. 2007, *ApJ*, 671, 1748
- Lee, J.-E., Di Francesco, J., Lai, S.-P., et al. 2006, *ApJ*, 648, 491
- Lee, J.-E., Lee, H.-G., Shinn, J.-H., et al. 2010, *ApJ*, 709, L74
- Lindberg, J. E., Jørgensen, J. K., Green, J. D., et al. 2014, *A&A*, 565, A29
- Mamajek, E. E. 2009, in *American Institute of Physics Conference Series*, Vol. 1158, American Institute of Physics
- Conference Series, ed. T. Usuda, M. Tamura, & M. Ishii, 3–10
- Merín, B., Jørgensen, J., Spezzi, L., et al. 2008, *ApJS*, 177, 551
- Peterson, D. E., Caratti o Garatti, A., Bourke, T. L., et al. 2011, *ApJS*, 194, 43
- Ribas, Á., Bouy, H., & Merín, B. 2015, *ArXiv e-prints*
- Ribas, Á., Merín, B., Bouy, H., & Maud, L. T. 2014, *A&A*, 561, A54
- Ridge, N. A., Di Francesco, J., Kirk, H., et al. 2006, *AJ*, 131, 2921
- Robitaille, T. P., Whitney, B. A., Indebetouw, R., Wood, K., & Denzmore, P. 2006, *ApJS*, 167, 256
- Soderblom, D. R., Hillenbrand, L. A., Jeffries, R. D., Mamajek, E. E., & Naylor, T. 2014, *Protostars and Planets VI*, 219
- Spezzi, L., Cox, N. L. J., Prusti, T., et al. 2013, *A&A*, 555, A71
- van Kempen, T. A., van Dishoeck, E. F., Salter, D. M., et al. 2009, *A&A*, 498, 167
- Vilas-Boas, J. W. S., Myers, P. C., & Fuller, G. A. 1994, *ApJ*, 433, 96

Table 4
HCO⁺ $J = 3 \rightarrow 2$ Detection Statistics for Clouds^a

Cloud (1)	D (pc) (2)	Size (pc) (3)	0+I Y (4)	0+I N (5)	Flat Y (6)	Flat N (7)	II Y (8)	II N (9)	V (km s ⁻¹) (10)	ΔV (km s ⁻¹) (11)	Number Stg 0+1 ^b (12)	Notes (13)
Aquila	260	7.56	66	15	39	21	13	26	7.4	3.0	97	
Auriga/CMC	450	5.98	28	5	5	3	6	1	0.9	1.8	30	
Auriga North	450	1.31	1	0	0	0	0	0	-6.9	1.9	1	
Cepheus 1	300	1.75	5	0	2	1	0	1	-4.4	1.3	5	stronger
									-2.9	1.0		weaker
Cepheus 3	288	1.75	4	2	0	1	0	1	2.6	1.3	4	
Cepheus 4	325	1.08	0	0	0	1	0	0	0	
Cepheus 5	200	1.07	0	0	3	0	0	0	-8.0	1.4	3	
Chamaeleon I	150	1.30	3	1	1	4	2	5	4.8	1.7	2	
Chamaeleon II	178	1.78	1	1	0	0	1	0	2.9	0.8	1	
Corona Australis (CrA)	130	0.98	5	1	2	2	0	1	5.2	2.9	7	
IC5146 E	950	4.42	8	5	0	2	0	3	6.5	1.2	7	
									8.1	1.3		stronger
IC5146 NW	950	5.28	13	0	3	1	0	0	4.2	2.0	11	
Lupus I	150	1.68	0	1	0	2	0	0	4.9	0.8	0	
Lupus III	200	2.22	1	1	0	5	0	1	1	
Lupus IV	150	0.90	0	1	0	0	0	0	0	
Lupus VI	150	1.46	0	1	0	0	0	0	0	
Musca	160	1.47	0	1	0	0	0	0	0	
Ophiuchus	125	3.08	24	3	26	14	1	2	3.1	1.8	45	stronger
									4.6	1.3		
Perseus	250	4.83	66	7	18	16	1	0	5.3	2.0	77	
	250								7.8	2.7		stronger
Scorpius/OphN	130	...	0	1	0	1	0	0	0	
Serpens	429	3.92	15	2	13	2	4	1	7.6	2.1	28	stronger
									9.6	1.6		
Total ^c			240	48	112	76	28	42			319	
Fraction ^d			0.83	0.17	0.60	0.40	0.40	0.60			0.58	

Note. — Columns are : (1) Cloud Name; (2) Cloud Distance in parsec; (3) Average Cloud Size in parsec; (4) Number of detected Class 0+I sources; (5) Number of undetected Class 0+I sources; (6) Number of detected Flat SED sources; (7) Number of undetected Flat SED sources; (8) Number of detected Class II sources; (9) Number of undetected Class II sources; (10) Cloud velocity (see Section 5); (11) Cloud line width (see Section 5); (12) Number of cloud sources classified as Stage 0+1; (13) Comparative notes on average cloud HCO⁺ spectra.

^a Only clouds with at least 1 observed source are included in the table.

^b Counts only detections above the threshold value of integrated intensity.

^c Total number of sources separated by class that are detected or undetected or are classified as Stage 0+1.

^d Fraction of sources in each column compared to total number surveyed.

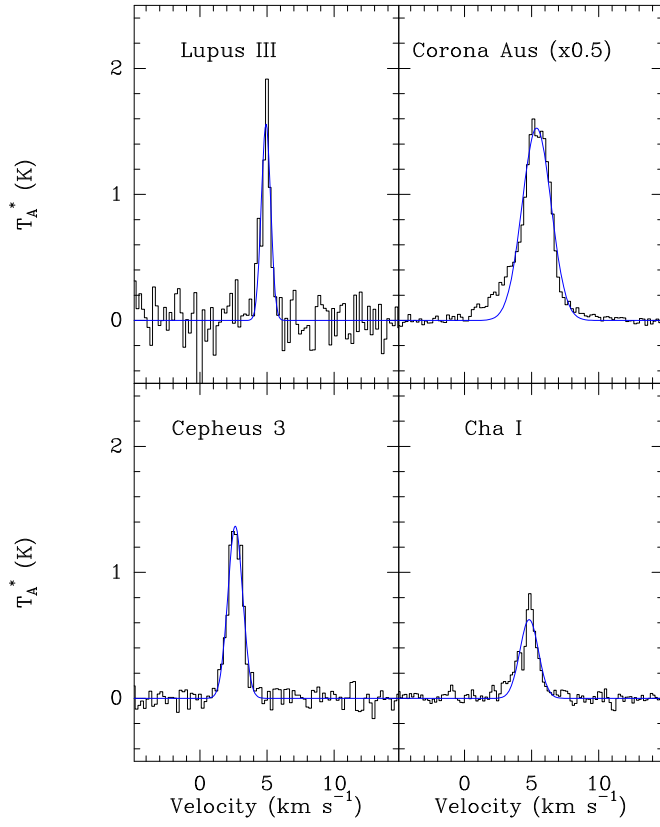


Figure 1. Average HCO^+ $J = 3 \rightarrow 2$ spectra of detected sources in four clouds. The black histogram is the average spectrum. The blue line is the fit to the spectrum (either one or two Gaussians). The spectrum of Corona Aus has been scaled down by a factor of 2.

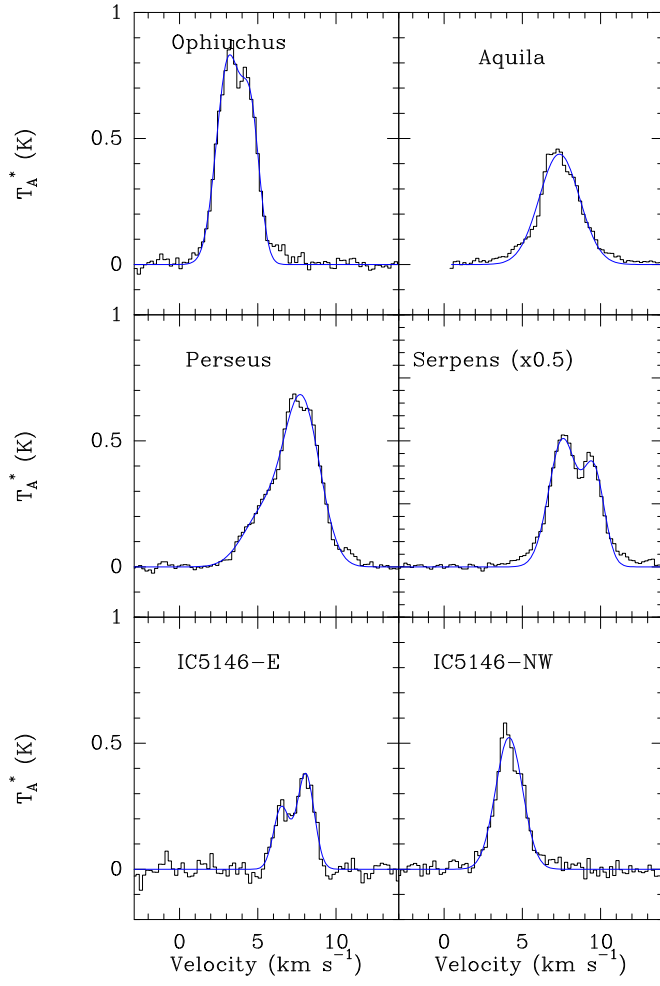


Figure 2. Average HCO^+ $J = 3 \rightarrow 2$ spectra of detected sources in six clouds. The black histogram is the average spectrum. The blue line is the fit to the spectrum (either one or two Gaussians).

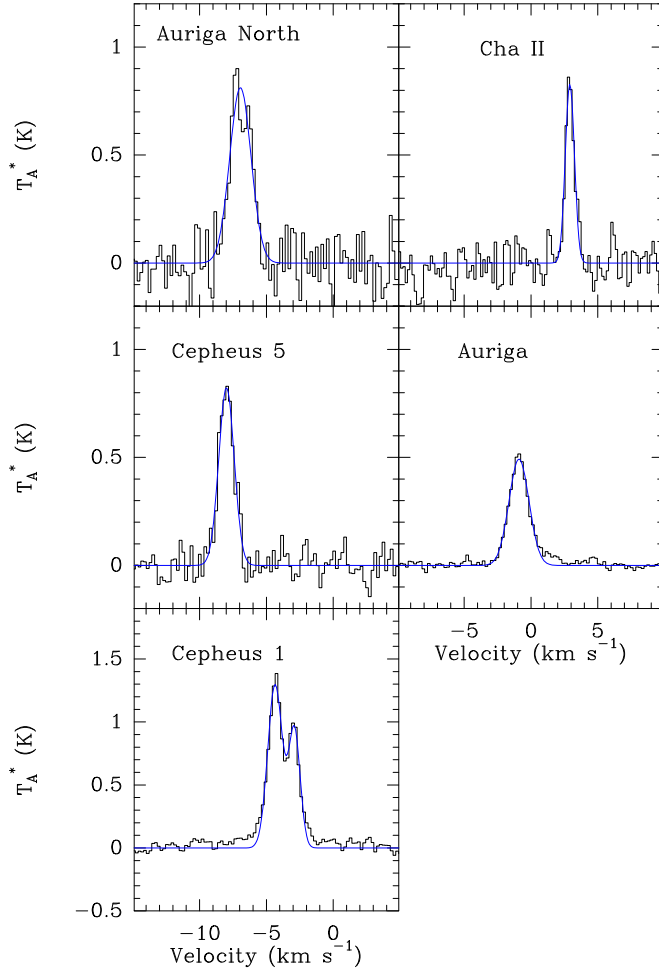


Figure 3. Average HCO^+ $J=3 \rightarrow 2$ spectra of detected sources in five clouds. The black histogram is the average spectrum. The blue line is the fit to the spectrum (either one or two Gaussians). The vertical scale for Cepheus 1 is larger than for other clouds.

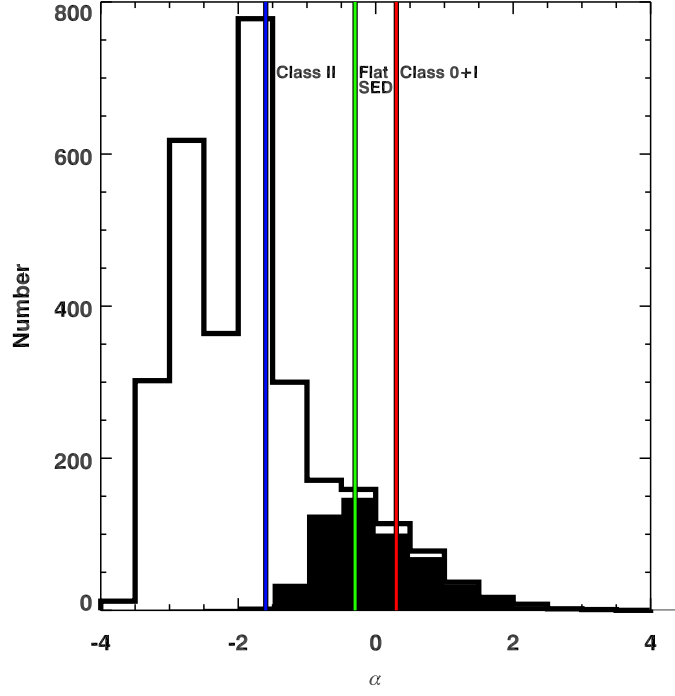


Figure 4. Distribution of α for the full catalog of YSOs (black line) and for the observed sample (filled). The vertical colored lines mark the boundaries between Class II and Class III ($\alpha = -1.6$), Class II and Flat ($\alpha = -0.3$), and Flat and Class 0+I ($\alpha = +0.3$).

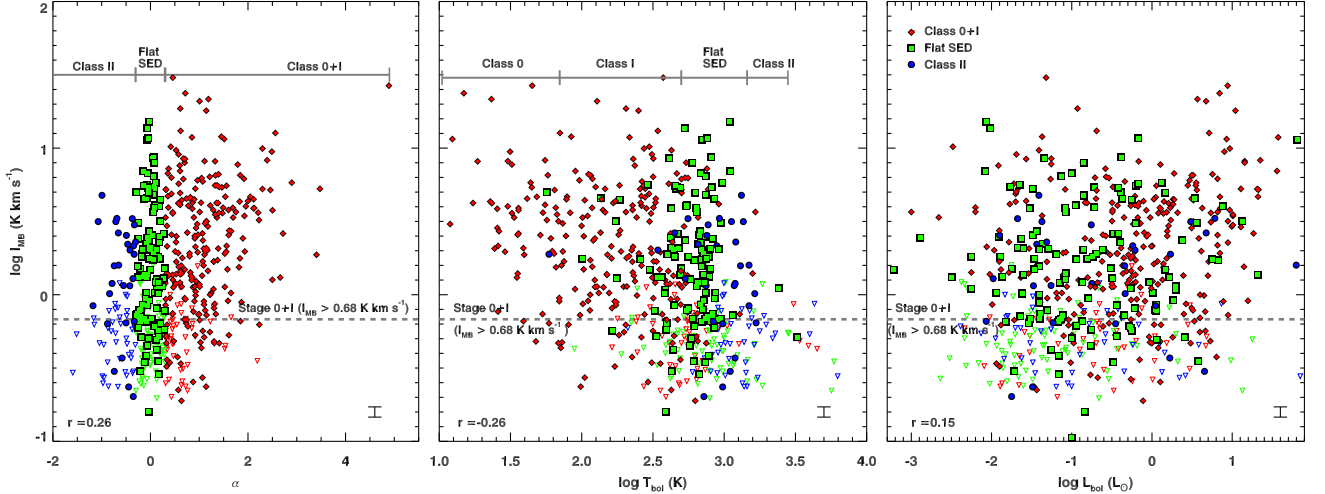


Figure 5. The integrated intensity of lines is shown versus α , T_{bol} , and L_{bol} , separated by Class as determined from α (Class 0+I, Flat SED, and Class II are red diamonds, green squares, and blue circle solid points, respectively). The left and middle panel show differences between using α and T_{bol} to classify sources (grey bars). Binned averages and their respective relations are shown by the yellow stars and errors. Pearson correlation coefficients and mean errors in I_{MB} are also shown (see §4.5). $\text{HCO}^+ J = 3 \rightarrow 2$ upper limits are shown as downward triangles.

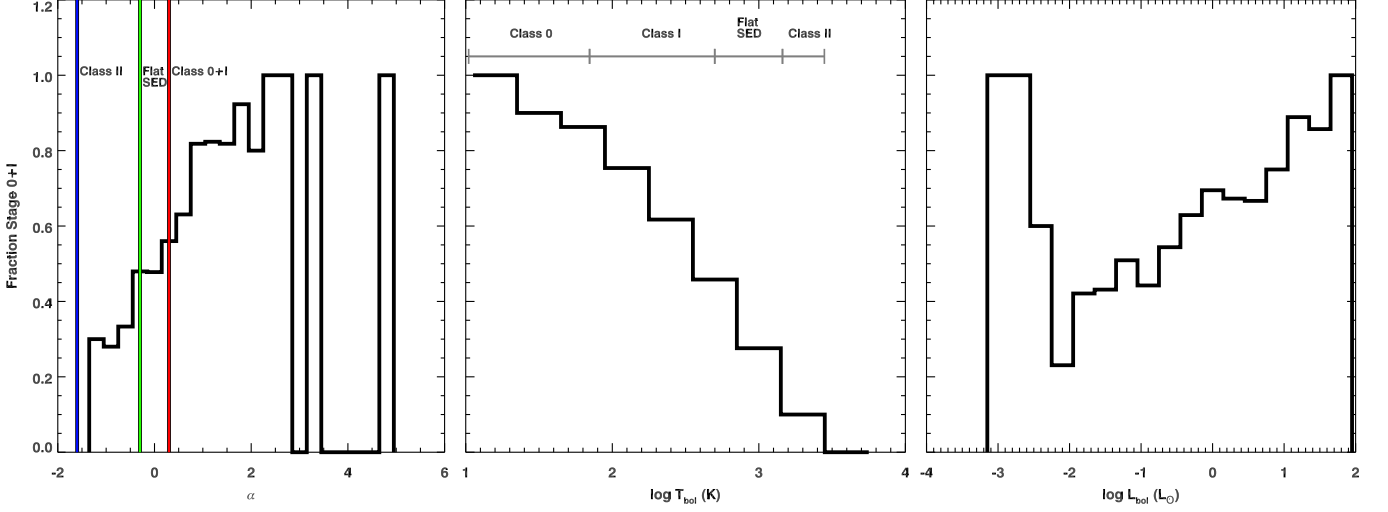


Figure 6. The fraction of Stage 0+I sources versus α , T_{bol} , and L_{bol} . The vertical colored lines in the left panel mark the boundaries between Class 0+I, Flat SED, and Class II protostars by α and the middle panel show these classification boundaries as defined by T_{bol} (grey bars). The bins plotted at zero fraction above $\alpha = 2$ have no sources, so the fraction is undefined. Every source with $\alpha > 2$ is detected. The peak at low values of L_{bol} is misleading as these bins suffer from very low number statistics.

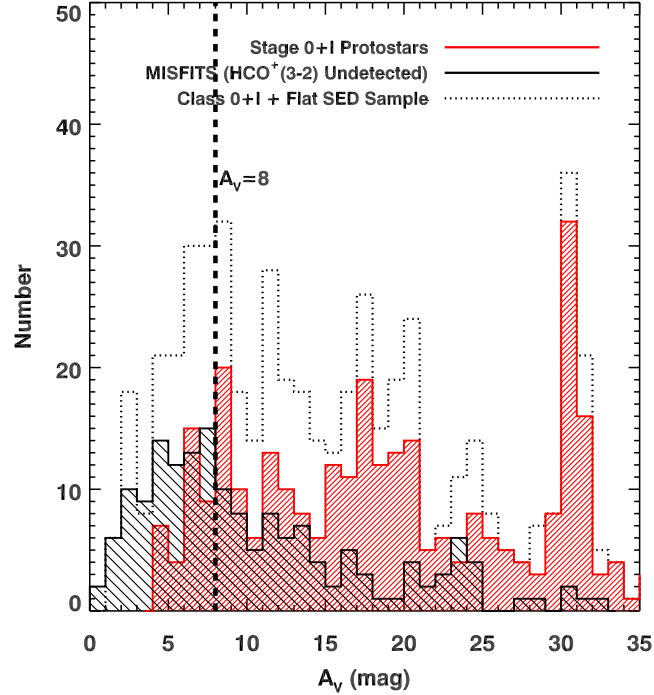


Figure 7. The number of sources that are SED Class 0+I or Flat (dotted line) compared to the distribution of Stage 0+I sources (red hashed histogram) and MISFITS (black hashed histogram). We find 89% of Stage 0+I protostars to lie above $A_V = 8$ mag (black vertical dashed line) compared to 75% of Class 0+I or Flat SED YSOs in the catalog. MISFITS are evenly distributed on either side of $A_V = 8$ mag.

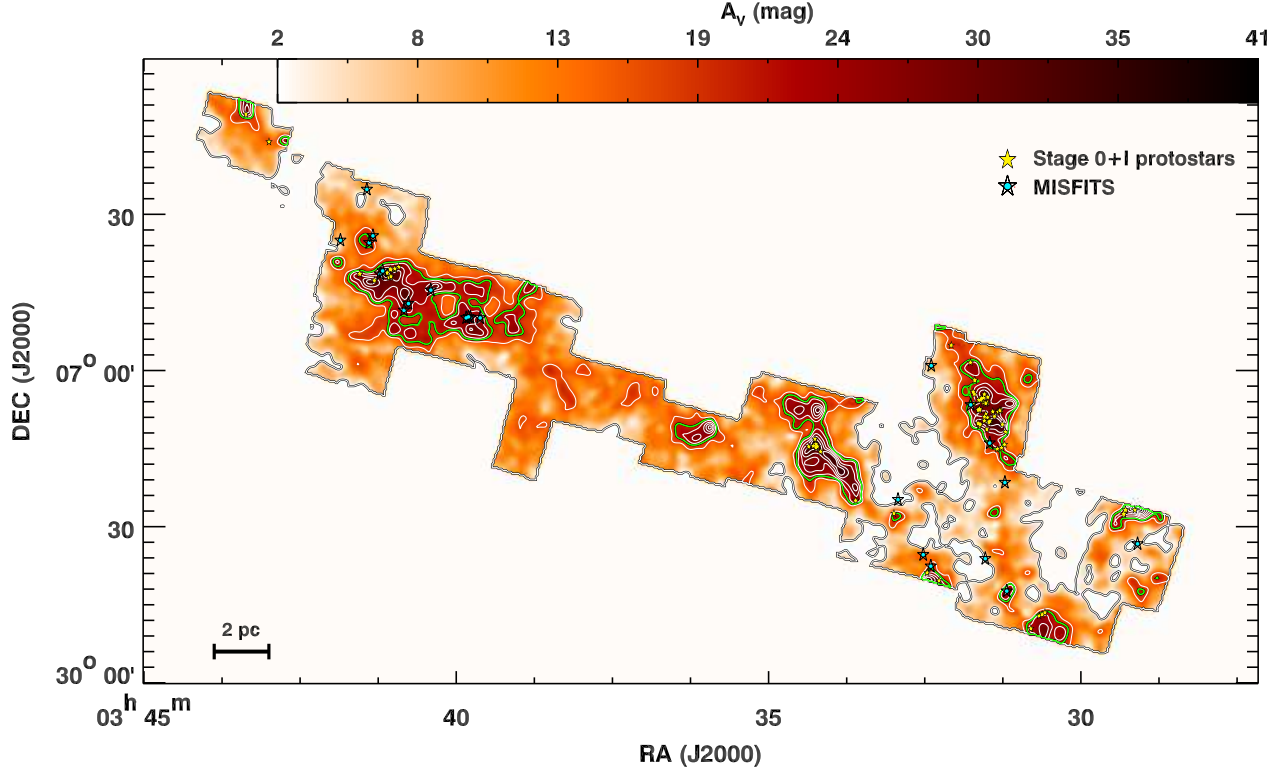


Figure 8. The distribution of bona fide Stage 0+I protostars and MISFITS in the Perseus molecular cloud. The background image is the $180''$ resolution extinction map with contours ranging from 2 to 41 mag in intervals of 4 mag. The black contour outlines the extinction map at the completeness limit of $A_V = 2$ mag and the green contour shows where $A_V = 8$ mag. The yellow stars are Stage 0+I protostars. Sources that are filled cyan circles and open stars correspond to MISFITS that are undetected in $\text{HCO}^+ J = 3 \rightarrow 2$ emission.

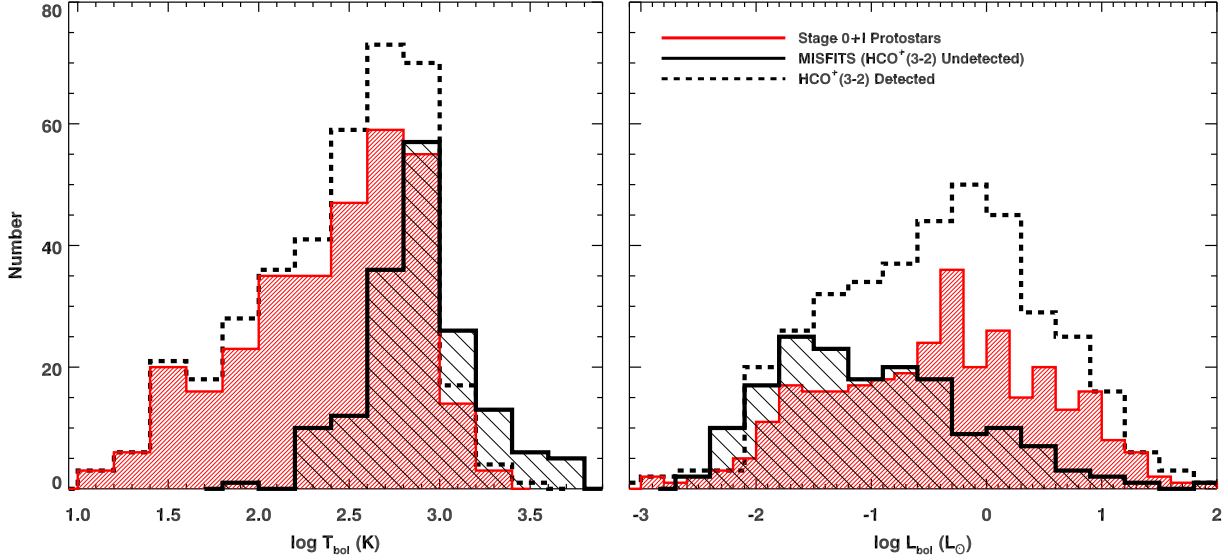


Figure 9. The number of MISFITS (undetected in $\text{HCO}^+ J = 3 \rightarrow 2$; hashed histogram) are compared to Class 0+1 and Flat SED YSOs that are detected in $\text{HCO}^+ J = 3 \rightarrow 2$ versus T_{bol} , and L_{bol} . Distributions are skewed to the right. The median values for T_{bol} and L_{bol} are 353 K and $0.43 L_{\odot}$ for Stage 0+I, 774 K and $0.083 L_{\odot}$ for MISFITS, and 330 K and $0.41 L_{\odot}$ for all detected YSO distribution, respectively.

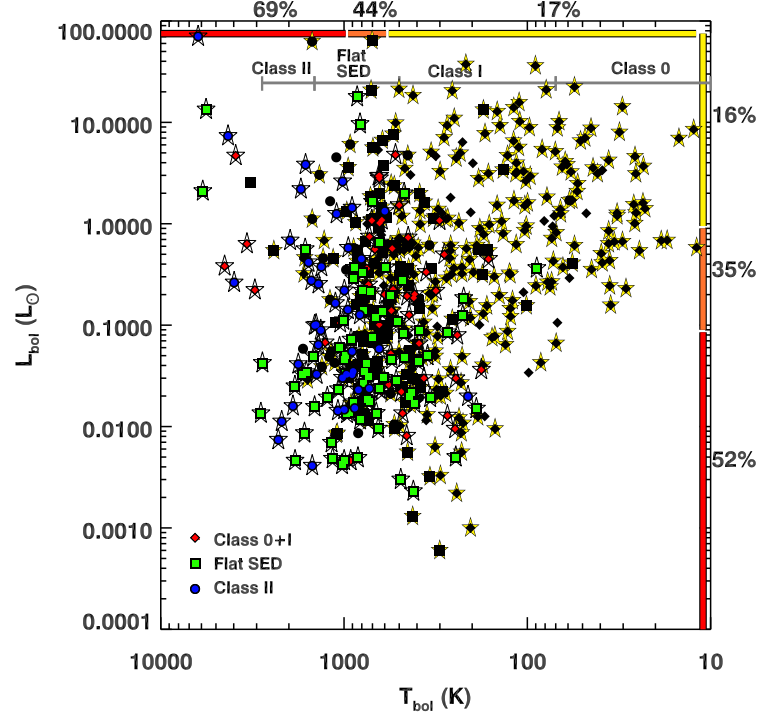


Figure 10. Bolometric luminosity (L_{bol}) is shown versus the bolometric temperature (T_{bol}) for all YSOs observed in $\text{HCO}^+ J = 3 \rightarrow 2$ separated by Class as determined from α (Class 0+I, Flat SED, and Class II are diamonds, squares, and circle solid points, respectively). Undetected YSOs or MISFITS are shown in color (Class 0+I, Flat SED, and Class II are red, green, and blue solid points, respectively) with an open star. Stage 0+I protostars are indicated by the yellow stars. The percent of YSO contamination defined as the number of MISFITS divided by the total surveyed in a bin is shown color coded from more (red) to less (yellow). Less contamination ($\leq 17\%$) is found where $T_{bol} \lesssim 600$ K and $L_{bol} \gtrsim 1 L_{\odot}$.

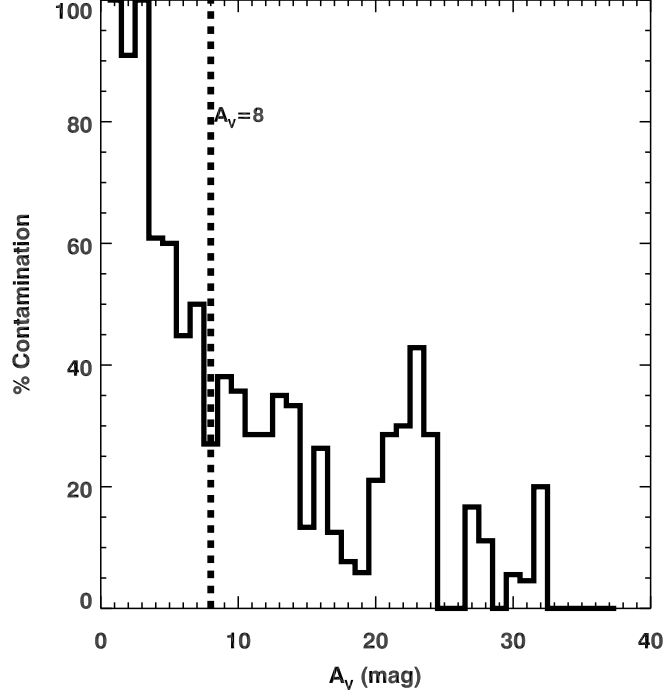


Figure 11. The percent of YSO contamination defined as the number of MISFITS (undetected in $\text{HCO}^+ J = 3 \rightarrow 2$) divided by the total number surveyed versus A_V . The contamination fraction is $> 90\%$ at $A_V < 4$ mag and decreases as A_V increases. The rise above $A_V = 20$ mag is due to low number statistics.

APPENDIX

RESULTS ON SOURCES

The full list of sources with HCO^+ observations is given in Table 5, along with their spectral index, α , after extinction correction, as described in Dunham et al. (2013), and the resulting SED class.

NOTES ON CLOUDS

Aquila

Many spectra had two velocity components which could be separated in some positions, but not all. Emission also moved in velocity over a range of 3 to 10 km s^{-1} . The two components are not apparent in the average spectrum in figure 2; instead they blend into a single, rather broad (3.0 km s^{-1}) component (Table 4). The Spitzer data on this cloud were analyzed by Gutermuth et al. (2008), and a preliminary analysis of the *Herschel* data can be found in Bontemps et al. (2010).

Auriga

This cloud is also called the California Molecular Cloud. There are at least two velocity components, one near -1 km s^{-1} and another near -4.5 km s^{-1} , along with a possible third component around 1.5 km s^{-1} . Only the component centered near -1 km s^{-1} is strong and fitted in the average spectrum in figure 3. For the most part, each position shows one component, but in a few positions, both were present and two Gaussians were fitted. The Spitzer data were published by Broekhoven-Fiene et al. (2014) and *Herschel* imaging by Harvey et al. (2013). A single source was observed in Auriga North, and its spectrum in figure 3 shows that it has a quite different velocity -6.9 km s^{-1} from the main Auriga cloud.

Cepheus clouds

Most of these clouds tended to have a single velocity component in the range of 1-5 km s^{-1} . Cepheus 1 had two components in some positions, both in the range of -5 to -3 km s^{-1} , but these could also be self-absorbed spectra from a single component. We have fitted the average spectrum for Cepheus 1 with two components (Fig. 3). The average spectra of the other two clouds with detections (Fig. 3 for Cepheus 5; Fig. 1 for Cepheus 3) show relatively narrow lines, and they were fitted by a single Gaussian (Table 4). Cepheus 5 had a line centered at -7.8 km s^{-1} , while the line in Cepheus 3 is centered at $+2.5 \text{ km s}^{-1}$. The Spitzer data for these clouds have been analyzed by Kirk et al. (2009). The YSOs in Cepheus 1 are associated with L1251A and L1251B. These regions have been analyzed in detail (Lee et al. 2006, 2007, 2010) showing that the $\text{HCO}^+ J = 3 \rightarrow 2$ spectrum is self-reversed toward the collection of YSOs, so the two components in our average spectrum are most likely not separate components but instead manifestations of a self-reversed profile.

Chamaeleon Clouds

The Cha I cloud showed two possible velocity features, but they were not very apparent in the average spectrum, which was not well fitted by a single Gaussian (Fig. 1). However attempts to fit two Gaussians did not produce believable results. The components were always close together and could be simply self reversed profiles of a single component. The Cha II cloud had a single narrow component at the two positions with detections. The average spectrum is in figure 3. The Spitzer data for Cha II were published by Alcalá et al. (2008) and *Herschel* data on Cha II have been analyzed by Spezzi et al. (2013).

Corona Australis

This cloud exhibits one primary velocity component, but some lines were self-absorbed and/or showed broad wings. The average spectrum (Fig. 1) shows some structure, but only a single component could be easily fitted. The *Spitzer* data on this cloud have been published by Peterson et al. (2011), and a detailed analysis of the main sources with data from *Herschel* is presented by Lindberg et al. (2014).

IC5146

This region has two cloud sections, IC5146-NW and IC5146-E. IC5146-NW has a single velocity component centered around 4 km s^{-1} . The average spectrum (Fig. 2) was fitted with a single component, although there is clearly some non-Gaussian structure. The average spectrum for IC5146-E was fitted with two components, one at 6.5 km s^{-1} , and stronger one at 8 km s^{-1} . The Spitzer data have been published by Harvey et al. (2008).

Lupus

The Lupus region contains 6 clouds, usually denoted by roman numerals (Comerón 2008). The only source detected in HCO^+ was in Lupus III (Fig. 1). The velocity from that detection was used to set upper limits on the other sources. The Spitzer data were published by Merín et al. (2008).

Musca

No line was detected toward the Musca cloud, so the upper limits are based on the velocity range of ^{13}CO emission in Vilas-Boas et al. (1994).

Ophiuchus

Many spectra had two velocity components which could be separated in some positions, but not all. Both components also moved in velocity over a range of 2.5 to 5 km s⁻¹. The average spectrum (Fig. 2) has been fitted with two components (Table 4), and there is also a shoulder on the high-velocity side of the spectrum. This cloud was mapped in CO and ¹³CO by Ridge et al. (2006), who provided fits to their cloud averaged spectra. The mean velocity for both species was 3.38 km s⁻¹, with linewidths of 2.77 km s⁻¹ for CO and 2.38 km s⁻¹ for ¹³CO. Both linewidths are substantially larger than those of our individual components and may represent blends. Their average spectra are consistent with our two components, but they were too blended to fit separately.

Perseus

Two components are seen in the spectra of many positions. They are quite blended in the average spectrum (Fig. 2, but two components could be fitted. This spectrum is broadly consistent with an average spectrum of ¹³CO in Ridge et al. (2006), which is however more blended. Their spectrum shows a third peak around 0 km s⁻¹, which may appear weakly in our average spectrum. Ridge et al. (2006) also note a velocity gradient from east to west across the cloud.

Serpens

Many spectra had two velocity components (7.6 and 9.6 km s⁻¹), which could be separated in some positions, but not all. Both components also moved in velocity over a range of 7 to 8 and 8 to 10 km s⁻¹, respectively. The average spectrum (Fig. 2) was fitted with two components (Table 4, and there is weak shoulder extending to higher velocity.

Table 5
MISFITS Properties

Cloud Name (1)	Source Name (2)	RA _{obs} (J2000) (3)	DEC _{obs} (J2000) (4)	$\alpha_{E.C.}$ (5)	$\int T_{MB} dV$ (K km s ⁻¹) (6)	$\int T_{MB} dV$ (K km s ⁻¹) (7)	V (km s ⁻¹) (8)	ΔV (km s ⁻¹) (9)	V (km s ⁻¹) (10)	ΔV (km s ⁻¹) (11)	A_V (Mag) (12)	SMM (Y/N) (13)	Stg 0+I (Y/N) (14)
Aquila	J180444.5-043706	18:04:44.52	-04:37:06.02	-0.10	<0.63						13.7		N
Aquila	J180531.1-043809	18:05:31.11	-04:38:09.63	-0.00	<0.33						9.1		N
Aquila	J181028.9-023742	18:10:28.90	-02:37:42.79	-0.12	<0.50						5.8		N
Aquila	J182632.8-034627	18:26:32.81	-03:46:27.26	-0.17	<0.41						10.3		N
Aquila	J182703.3-024533	18:27:03.33	-02:45:33.42	0.13	<0.26						5.2		N
Aquila	J182713.2-034014	18:27:13.23	-03:40:14.57	-0.96	<0.46						12.1		N
Aquila	J182736.7-035004	18:27:36.71	-03:50:04.71	0.41	<0.66						16.4		N
Aquila	J182754.7-034238	18:27:54.73	-03:42:38.57	0.38	1.35±0.16		6.36±0.08	1.32±0.20			20.9		Y
Aquila	J182805.4-034659	18:28:05.41	-03:46:59.82	0.80	1.83±0.10		7.46±0.04	1.24±0.09			22.9		Y
Aquila	J182809.4-022631	18:28:09.49	-02:26:31.95	-1.15	<0.63						4.7		N
Aquila	J182842.6-012951	18:28:42.69	-01:29:51.00	-0.48	<0.98						14.0		N
Aquila	J182847.7-013807	18:28:47.75	-01:38:07.95	1.52	1.13±0.12		6.65±0.02	0.45±0.06			18.2		Y
Aquila	J182847.7-013814	18:28:47.78	-01:38:14.49	0.33	1.40±0.12		6.62±0.02	0.50±0.06			18.2		Y
Aquila	J182854.8-013727	18:28:54.88	-01:37:27.17	0.82	1.42±0.11		7.52±0.04	1.10±0.09			21.3		Y
Aquila	J182855.8-013734	18:28:55.84	-01:37:34.93	0.61	1.21±0.11		7.48±0.05	1.16±0.12			22.5		Y
Aquila	J182855.8-014313	18:28:55.84	-01:43:13.66	0.02	<0.52						20.9		N
Aquila	J182857.1-013715	18:28:57.14	-01:37:15.24	-0.12	0.69±0.12		7.62±0.06	1.01±0.29			21.3		Y
Aquila	J182858.3-013834	18:28:58.35	-01:38:34.54	0.29	1.52±0.13		7.51±0.03	0.81±0.09			23.8		Y
Aquila	J182901.8-013902	18:29:01.83	-01:39:02.77	-0.13	1.37±0.15		7.15±0.04	0.81±0.12			24.8		Y
Aquila	J182905.3-014156	18:29:05.32	-01:41:56.74	0.96	6.03±0.18		7.91±0.02	1.45±0.06			25.7	N	Y
Aquila	J182905.4-034245	18:29:05.45	-03:42:45.60	0.07	1.74±0.13	0.61±0.13	5.23±0.05	1.21±0.10	8.97±0.14	1.26±0.26	15.2		Y
Aquila	J182905.9-013025	18:29:05.92	-01:30:25.12	0.75	0.62±0.11	0.68±0.12	7.56±0.19	1.03±0.25	7.57±0.13	1.03±0.21	20.3		N
Aquila	J182908.0-020221	18:29:08.01	-02:02:21.80	0.19	<0.78						17.4		N
Aquila	J182908.1-020538	18:29:08.17	-02:05:38.48	0.06	1.90±0.14		6.11±0.03	0.80±0.06			19.3		Y
Aquila	J182911.2-020430	18:29:11.19	-02:04:30.66	0.33	0.47±0.11		6.20±0.13	0.90±0.27			19.5		N
Aquila	J182912.1-014845	18:29:12.11	-01:48:45.40	-0.33	<0.59						20.5		N
Aquila	J182912.8-020350	18:29:12.83	-02:03:50.48	1.07	0.57±0.11		6.19±0.23	2.60±0.73			19.1		N
Aquila	J182913.0-014617	18:29:13.07	-01:46:17.08	0.62	1.45±0.13		6.85±0.03	0.72±0.07			22.0		Y
Aquila	J182916.6-020339	18:29:16.63	-02:03:39.73	-0.06	<0.48						17.8		N
Aquila	J182916.7-011736	18:29:16.72	-01:17:36.92	-0.88	<0.35						9.7		N
Aquila	J182916.8-011730	18:29:16.80	-01:17:30.68	0.65	<0.26						9.7		N
Aquila	J182920.9-013714	18:29:20.98	-01:37:14.22	0.13	0.81±0.13		7.67±0.13	1.57±0.28			19.6		Y
Aquila	J182923.4-013855	18:29:23.41	-01:38:55.64	1.07	1.69±0.09		8.06±0.03	1.25±0.08			20.0	N	Y
Aquila	J182925.1-014737	18:29:25.12	-01:47:37.90	0.13	0.42±0.06		7.68±0.06	0.99±0.19			25.7		N
Aquila	J182936.6-015059	18:29:36.69	-01:50:59.22	0.11	5.81±0.11		8.05±0.02	1.99±0.04			29.6		Y
Aquila	J182937.4-031453	18:29:37.43	-03:14:53.90	-0.03	0.16±0.04		6.28±0.10	0.79±0.24			10.5		N
Aquila	J182938.1-015100	18:29:38.12	-01:51:00.56	1.07	5.92±0.14		8.11±0.03	2.13±0.06			28.9	N	Y
Aquila	J182938.7-015100	18:29:38.70	-01:51:00.48	0.64	4.41±0.10		8.07±0.02	2.07±0.05			28.9	N	Y
Aquila	J182939.1-015021	18:29:39.18	-01:50:21.67	-0.08	1.31±0.14		7.91±0.10	1.84±0.26			29.2		Y
Aquila	J182940.2-015127	18:29:40.25	-01:51:27.96	-0.49	2.54±0.17		7.82±0.06	1.74±0.13			28.1		Y
Aquila	J182940.2-014032	18:29:40.28	-01:40:32.12	0.74	<0.41						12.4		N
Aquila	J182941.6-015129	18:29:41.61	-01:51:29.33	-0.79	1.19±0.15		7.43±0.10	1.70±0.33			28.1		Y
Aquila	J182941.9-015011	18:29:41.92	-01:50:11.56	0.45	1.37±0.08		7.90±0.02	0.94±0.07			27.6	N	Y
Aquila	J182943.3-015651	18:29:43.33	-01:56:51.89	0.93	1.05±0.11		7.44±0.09	1.63±0.16			28.2	N	Y
Aquila	J182943.9-021255	18:29:43.96	-02:12:55.32	1.29	1.09±0.07		7.78±0.02	0.75±0.05			17.8		Y
Aquila	J182945.9-013312	18:29:45.96	-01:33:12.62	-0.06	<0.70						12.9		N
Aquila	J182947.0-015548	18:29:47.01	-01:55:48.14	0.29	0.78±0.09		7.44±0.07	1.20±0.16			30.2	N	Y
Aquila	J182947.3-015603	18:29:47.34	-01:56:03.72	0.32	0.76±0.08		7.53±0.06	1.00±0.13			30.2		Y
Aquila	J182952.1-015736	18:29:52.15	-01:57:36.93	1.01	0.67±0.06		7.76±0.06	1.37±0.12			31.5		N
Aquila	J182952.3-015745	18:29:52.34	-01:57:45.75	0.62	0.34±0.09		8.11±0.06	0.55±0.20			31.9		N
Aquila	J182953.7-015746	18:29:53.76	-01:57:46.90	-0.09	0.65±0.10		7.34±0.10	1.21±0.21			31.9		N
Aquila	J182954.3-015823	18:29:54.37	-01:58:23.40	0.31	<0.25						31.9		N
Aquila	J182957.0-015945	18:29:57.08	-01:59:45.91	-0.36	1.29±0.16		6.81±0.07	1.22±0.19			31.8		Y

Table 5 — Continued

Cloud Name (1)	Source Name (2)	RA _{obs} (J2000) (3)	DEC _{obs} (J2000) (4)	$\alpha_{E.C.}$ (5)	$\int T_{MB} dV$ (K km s ⁻¹) (6)	$\int T_{MB} dV$ (K km s ⁻¹) (7)	V (km s ⁻¹) (8)	ΔV (km s ⁻¹) (9)	V (km s ⁻¹) (10)	ΔV (km s ⁻¹) (11)	A_V (Mag) (12)	SMM (Y/N) (13)	Stg 0+I (Y/N) (14)
Aquila	J182957.9-020103	18:29:57.92	-02:01:03.23	-0.26	1.57±0.15	1.00±0.14	6.89±0.04	0.94±0.12	8.28±0.06	0.86±0.14	31.2		Y
Aquila	J182958.3-015740	18:29:58.35	-01:57:40.23	1.14	0.24±0.04		8.28±0.04	0.41±0.08			28.9		N
Aquila	J182958.9-020125	18:29:58.94	-02:01:25.53	0.53	2.28±0.15	1.42±0.14	6.97±0.04	1.27±0.09	8.57±0.05	1.07±0.12	31.2		Y
Aquila	J182959.0-020157	18:29:59.02	-02:01:57.38	-0.02	1.76±0.25	1.49±0.25	6.76±0.05	0.96±0.11	8.09±0.11	1.31±0.22	30.7		Y
Aquila	J182959.4-020106	18:29:59.47	-02:01:06.35	0.53	1.68±0.14	1.27±0.16	6.87±0.04	0.96±0.08	8.45±0.07	1.27±0.20	31.2	N	Y
Aquila	J183000.0-015715	18:30:00.07	-01:57:15.69	0.19	<0.40						28.9		N
Aquila	J183000.2-020052	18:30:00.22	-02:00:52.42	0.70	1.48±0.10	0.62±0.11	6.70±0.03	0.88±0.07	8.34±0.04	0.57±0.15	31.2		Y
Aquila	J183000.5-020211	18:30:00.56	-02:02:11.27	0.08	3.92±0.20	1.28±0.20	6.77±0.03	1.16±0.07	8.41±0.07	1.00±0.20	30.7		Y
Aquila	J183000.6-020204	18:30:00.67	-02:02:04.69	0.06	3.65±0.29	1.40±0.31	6.74±0.04	1.16±0.07	8.23±0.14	1.43±0.39	30.7		Y
Aquila	J183001.0-020608	18:30:01.07	-02:06:08.88	0.34	2.14±0.96	1.11±0.88	7.42±0.34	1.70±0.26	8.11±0.06	0.88±0.28	32.6	N	Y
Aquila	J183001.1-020127	18:30:01.12	-02:01:27.65	-0.37	3.30±0.19		6.91±0.03	1.00±0.08			31.4		Y
Aquila	J183001.2-020148	18:30:01.25	-02:01:48.26	0.46	3.58±0.48	1.63±0.50	6.84±0.04	1.11±0.07	7.95±0.35	2.20±0.51	31.0		Y
Aquila	J183001.3-020609	18:30:01.25	-02:06:03.74	-1.07	3.15±0.15		7.71±0.04	1.72±0.09			32.6		Y
Aquila	J183001.3-020342	18:30:01.32	-02:03:42.92	1.32	5.56±0.16		7.30±0.03	2.21±0.07			31.1		Y
Aquila	J183002.2-020159	18:30:02.26	-02:01:59.26	0.43	6.29±0.24		6.82±0.02	1.25±0.06			31.0		Y
Aquila	J183002.4-020257	18:30:02.45	-02:02:57.88	0.36	4.46±0.22	6.72±0.23	6.38±0.03	1.54±0.09	8.47±0.02	1.30±0.06	30.9	N	Y
Aquila	J183002.7-020259	18:30:02.76	-02:02:59.64	0.08	4.72±0.20	7.93±0.23	6.37±0.03	1.33±0.07	8.49±0.02	1.45±0.06	31.1		Y
Aquila	J183002.8-020240	18:30:02.84	-02:02:40.49	0.71	4.36±0.21	8.43±0.30	6.40±0.03	1.30±0.06	8.68±0.03	2.05±0.10	30.9		Y
Aquila	J183002.8-020222	18:30:02.85	-02:02:22.55	0.43	4.88±0.23	4.31±0.33	6.63±0.02	1.04±0.05	8.61±0.06	1.87±0.19	30.9		Y
Aquila	J183003.0-020133	18:30:03.00	-02:01:33.12	-0.18	1.81±0.23	1.10±0.25	6.77±0.04	0.88±0.10	8.13±0.15	1.34±0.32	31.0		Y
Aquila	J183003.1-013632	18:30:03.10	-01:36:32.63	0.91	2.52±0.22		8.22±0.03	0.77±0.08			13.0		Y
Aquila	J183003.1-020234	18:30:03.17	-02:02:34.81	0.58	5.03±0.42	9.06±0.48	6.52±0.05	1.41±0.15	8.82±0.04	1.78±0.12	30.9		Y
Aquila	J183003.2-020326	18:30:03.23	-02:03:26.34	0.67	7.78±0.94	8.48±1.21	6.46±0.05	1.49±0.11	8.68±0.11	2.54±0.41	31.1		Y
Aquila	J183003.3-020245	18:30:03.38	-02:02:45.45	0.62	5.14±0.08	13.11±0.66	6.46±0.04	1.46±0.10	8.94±0.04	2.16±0.14	30.9		Y
Aquila	J183004.3-020138	18:30:04.39	-02:01:38.23	0.31	3.36±0.21		7.45±0.08	2.60±0.18			30.6		Y
Aquila	J183004.4-020415	18:30:04.47	-02:04:15.78	-0.06	6.71±0.19		7.18±0.03	2.03±0.06			31.3		Y
Aquila	J183004.7-020227	18:30:04.79	-02:02:27.84	0.37	3.93±0.60	3.67±0.50	6.51±0.12	2.17±0.44	8.85±0.09	1.58±0.20	30.6		Y
Aquila	J183004.9-020142	18:30:04.97	-02:01:42.49	0.10	4.09±0.17		7.49±0.05	2.89±0.15			30.6		Y
Aquila	J183005.1-020141	18:30:05.17	-02:01:41.56	-0.00	2.03±0.17		7.49±0.09	2.19±0.20			30.6		Y
Aquila	J183005.2-020206	18:30:05.23	-02:02:06.39	-0.10	2.07±0.18		7.77±0.10	2.19±0.21			30.6		Y
Aquila	J183005.2-020234	18:30:05.28	-02:02:34.11	-0.13	4.52±0.37		7.84±0.15	4.06±0.43			30.6		Y
Aquila	J183005.2-020325	18:30:05.29	-02:03:25.89	0.53	9.67±0.14		6.96±0.01	1.89±0.03			30.8		Y
Aquila	J183005.5-020107	18:30:05.52	-02:01:07.98	0.16	1.02±0.09	1.01±0.16	6.74±0.02	0.39±0.04	8.14±0.09	1.19±0.26	30.9		Y
Aquila	J183005.8-020144	18:30:05.79	-02:01:58.07	1.18	0.00±0.09	2.92±0.09	7.76±0.20	1.29±0.20	7.74±0.20	3.08±0.20	30.6		Y
Aquila	J183006.0-011019	18:30:06.06	-01:10:19.33	-0.40	<0.37						6.3		N
Aquila	J183006.2-020219	18:30:06.20	-02:02:19.57	-0.47	2.21±0.24		7.78±0.12	2.59±0.40			30.6		Y
Aquila	J183006.2-020304	18:30:06.25	-02:03:04.08	0.58	5.72±0.23		7.29±0.05	2.53±0.12			30.8		Y
Aquila	J183006.8-020337	18:30:06.80	-02:03:37.47	0.07	5.30±0.18		6.95±0.02	1.34±0.06			30.8		Y
Aquila	J183008.7-020610	18:30:08.72	-02:06:10.03	0.00	2.09±0.19		7.07±0.08	1.70±0.16			31.4		Y
Aquila	J183010.8-020354	18:30:10.80	-02:03:54.69	-0.09	2.23±0.15		7.20±0.05	1.65±0.13			29.6		Y
Aquila	J183011.3-020656	18:30:11.32	-02:06:56.84	0.92	2.12±0.15		6.74±0.04	1.34±0.12			30.3		Y
Aquila	J183013.0-012536	18:30:13.01	-01:25:36.64	-0.95	<0.27						7.9		N
Aquila	J183015.6-020719	18:30:15.63	-02:07:19.60	0.91	2.42±0.15		6.85±0.05	1.39±0.09			29.7		Y
Aquila	J183015.6-015035	18:30:15.68	-01:50:35.21	-0.30	2.29±0.17		7.91±0.05	1.42±0.13			22.3		Y
Aquila	J183016.2-015252	18:30:16.24	-01:52:52.94	0.40	0.95±0.09		6.65±0.05	1.10±0.14			25.1		Y
Aquila	J183016.7-022936	18:30:16.70	-02:29:36.97	0.17	<0.88						11.2		N
Aquila	J183017.0-020958	18:30:17.01	-02:09:58.71	0.97	1.95±0.15		7.06±0.05	1.17±0.10			25.1		Y
Aquila	J183017.4-020958	18:30:17.47	-02:09:58.45	1.11	1.87±0.12		6.98±0.04	1.30±0.09			25.1	N	Y
Aquila	J183021.2-021112	18:30:21.28	-02:11:12.39	-0.01	<0.54						23.9		N
Aquila	J183021.8-015200	18:30:21.82	-01:52:00.99	-0.07	0.85±0.09		7.25±0.05	1.06±0.14			24.3		Y
Aquila	J183021.9-020912	18:30:21.93	-02:09:12.03	-0.42	1.15±0.06		5.02±0.10	3.87±0.20			26.7		Y
Aquila	J183024.1-021029	18:30:24.15	-02:10:29.55	-0.28	0.69±0.18		7.33±0.35	2.43±0.67			24.4		Y
Aquila	J183024.5-015410	18:30:24.57	-01:54:10.62	0.12	0.49±0.10		7.55±0.04	0.46±0.14			28.8	N	N
Aquila	J183025.7-021115	18:30:25.78	-02:11:15.25	0.77	0.61±0.10		7.42±0.05	0.63±0.11			23.4		N

Table 5 — Continued

Cloud Name (1)	Source Name (2)	RA _{obs} (J2000) (3)	DEC _{obs} (J2000) (4)	$\alpha_{E.C.}$ (5)	$\int T_{MB} dV$ (K km s ⁻¹) (6)	$\int T_{MB} dV$ (K km s ⁻¹) (7)	V (km s ⁻¹) (8)	ΔV (km s ⁻¹) (9)	V (km s ⁻¹) (10)	ΔV (km s ⁻¹) (11)	A_V (Mag) (12)	SMM (Y/N) (13)	Stg 0+I (Y/N) (14)
Aquila	J183025.8-021042	18:30:25.88	-02:10:42.93	1.22	0.69±0.09	1.00±0.11	6.17±0.06	0.90±0.13	7.91±0.07	1.34±0.19	24.5	N	Y
Aquila	J183025.9-021142	18:30:25.92	-02:11:42.16	0.64	0.19±0.06		7.18±0.12	0.48±0.23			23.4		N
Aquila	J183026.8-015327	18:30:26.84	-01:53:27.01	-0.08	0.38±0.06		7.26±0.06	0.70±0.16			28.6		N
Aquila	J183027.1-021056	18:30:27.12	-02:10:56.47	0.97	<1.57						24.5		N
Aquila	J183027.2-021100	18:30:27.28	-02:11:00.27	0.33	0.52±0.07		7.34±0.04	0.68±0.12			24.5		N
Aquila	J183027.5-015439	18:30:27.58	-01:54:39.31	0.64	1.13±0.09		7.32±0.06	1.35±0.11			30.0		Y
Aquila	J183027.9-021037	18:30:27.96	-02:10:37.46	-0.45	0.23±0.08		6.51±0.08	0.48±0.22			24.3		N
Aquila	J183029.0-020720	18:30:29.08	-02:07:20.38	-0.38	<0.58						27.0		N
Aquila	J183031.1-021032	18:30:31.11	-02:10:32.46	-0.86	<0.24						23.9		N
Aquila	J183031.5-021606	18:30:31.51	-02:16:06.60	-0.51	<1.00						20.7		N
Aquila	J183031.5-021136	18:30:31.55	-02:11:36.42	-0.63	<0.37						23.2		N
Aquila	J183031.7-015613	18:30:31.74	-01:56:13.30	0.28	<1.12						32.7		N
Aquila	J183032.4-035001	18:30:32.48	-03:50:01.21	-0.14	<0.24						8.8		N
Aquila	J183033.2-021125	18:30:33.25	-02:11:25.81	-0.48	<0.78						23.2		N
Aquila	J183036.3-030601	18:30:36.38	-03:06:01.39	0.05	<0.36						10.1		N
Aquila	J183037.5-020853	18:30:37.51	-02:08:53.69	0.48	<0.47						24.1		N
Aquila	J183037.6-020840	18:30:37.61	-02:08:40.19	0.47	<0.47						24.1		N
Aquila	J183038.3-020843	18:30:38.31	-02:08:43.37	0.72	<0.24						24.1		N
Aquila	J183046.9-015651	18:30:46.90	-01:56:51.22	0.63	1.58±0.37		7.92±0.14	1.26±0.37			27.8		Y
Aquila	J183046.9-015645	18:30:46.93	-01:56:45.56	0.87	1.12±0.21		7.87±0.11	1.14±0.24			27.8	N	Y
Aquila	J183048.7-015601	18:30:48.74	-01:56:01.72	0.80	1.91±0.32		8.15±0.14	1.56±0.25			27.7	N	Y
Aquila	J183048.8-020713	18:30:48.83	-02:07:13.55	-0.37	<0.29						22.5		N
Aquila	J183054.9-020401	18:30:54.95	-02:04:01.01	-1.05	<0.47						19.2		N
Aquila	J183100.2-020338	18:31:00.22	-02:03:38.50	-0.97	<0.25						18.8		N
Aquila	J183102.7-020959	18:31:02.75	-02:09:59.41	0.17	1.22±0.05	0.00±2.78	6.49±0.04	1.03±0.07	12.58±2.17	12.24±3.23	23.7		Y
Aquila	J183111.0-020600	18:31:11.09	-02:06:00.67	1.22	6.37±0.28		5.04±0.03	1.19±0.06			24.4		Y
Aquila	J183114.6-021144	18:31:14.61	-02:11:44.96	-0.61	<0.63						21.4		N
Aquila	J183115.0-020105	18:31:15.01	-02:01:05.21	-0.78	<0.65						22.2		N
Aquila	J183119.4-020739	18:31:19.46	-02:07:39.66	1.04	3.18±0.02	4.24±0.15	3.98±0.02	1.40±0.04	6.85±0.04	2.61±0.12	23.4		Y
Aquila	J183120.4-021553	18:31:20.45	-02:15:53.51	-0.81	<0.56						21.0		N
Aquila	J183121.3-015335	18:31:21.34	-01:53:35.40	-0.87	<0.59						23.8		N
Aquila	J183129.8-020744	18:31:29.81	-02:07:44.37	-0.58	0.37±0.09		4.45±0.15	1.44±0.56			19.9		N
Aquila	J183130.5-020055	18:31:30.56	-02:00:55.81	-0.21	0.30±0.04		5.27±0.05	0.78±0.12			23.0		N
Aquila	J183133.8-021229	18:31:33.85	-02:12:29.15	-0.07	<0.56						16.4		N
Aquila	J183134.5-021512	18:31:34.55	-02:15:12.10	-0.09	0.94±0.11		5.72±0.05	0.80±0.12			18.7		Y
Aquila	J183135.3-021254	18:31:35.33	-02:12:54.88	-0.85	<0.78						17.0		N
Aquila	J183135.9-021330	18:31:35.95	-02:13:30.57	0.31	<0.57						17.6		N
Aquila	J183136.1-021448	18:31:36.12	-02:14:48.56	1.38	1.72±0.18	1.22±0.21	5.75±0.03	0.85±0.07	7.22±0.13	1.64±0.33	18.3		Y
Aquila	J183137.5-020503	18:31:37.51	-02:05:03.57	-0.72	<0.80						22.4		N
Aquila	J183137.6-021455	18:31:37.61	-02:14:55.91	-0.33	3.00±0.12		6.59±0.04	1.92±0.08			17.5		Y
Aquila	J183140.4-020814	18:31:40.49	-02:08:14.98	-0.27	0.73±0.08		2.18±0.04	0.68±0.09			16.0		Y
Aquila	J183148.5-021737	18:31:48.52	-02:17:37.30	-0.55	1.15±0.12		7.31±0.05	0.91±0.12			17.3		Y
Aquila	J183152.1-020126	18:31:52.18	-02:01:26.09	1.36	4.23±0.12		7.19±0.01	1.09±0.04			26.8	N	Y
Aquila	J183152.4-020031	18:31:52.48	-02:00:31.97	0.02	0.69±0.08		7.09±0.07	1.38±0.21			26.7		Y
Aquila	J183201.5-023814	18:32:01.56	-02:38:14.24	-0.25	<0.30						14.8		N
Aquila	J183206.2-021725	18:32:06.23	-02:17:25.57	-0.66	<0.82						15.0		N
Aquila	J183213.1-015730	18:32:13.19	-01:57:30.15	0.73	0.64±0.10		7.48±0.09	1.04±0.18			23.0	N	N
Aquila	J183215.1-023453	18:32:15.18	-02:34:53.42	1.39	2.07±0.13		6.03±0.05	1.48±0.11			18.0		Y
Aquila	J183215.9-023443	18:32:15.97	-02:34:43.12	0.20	4.44±0.13		5.84±0.02	1.67±0.05			17.6		Y
Aquila	J183237.4-025045	18:32:37.42	-02:50:45.25	0.18	<0.64						11.6		N
Aquila	J183238.1-022905	18:32:38.12	-02:29:05.63	-0.67	<0.24						13.9		N
Aquila	J183242.4-024756	18:32:42.48	-02:47:56.51	-0.88	0.63±0.06		6.49±0.04	0.79±0.09			12.8		N
Aquila	J183245.6-024657	18:32:45.68	-02:46:57.61	0.72	<0.69						13.7		N
Aquila	J183303.4-020842	18:33:03.49	-02:08:42.53	0.76	<0.22						7.8		N

Table 5 — Continued

Cloud Name (1)	Source Name (2)	RA _{obs} (J2000) (3)	DEC _{obs} (J2000) (4)	$\alpha_{E.C.}$ (5)	$\int T_{MB} dV$ (K km s ⁻¹) (6)	$\int T_{MB} dV$ (K km s ⁻¹) (7)	V (km s ⁻¹) (8)	ΔV (km s ⁻¹) (9)	V (km s ⁻¹) (10)	ΔV (km s ⁻¹) (11)	A_V (Mag) (12)	SMM (Y/N) (13)	Stg 0+I (Y/N) (14)
Aquila	J183323.7+004042	18:33:23.78	00:40:42.77	0.81	4.52±0.21		9.38±0.02	1.17±0.07			8.1		Y
Aquila	J183324.1+004036	18:33:24.18	00:40:36.74	1.41	5.44±0.22		9.36±0.02	1.20±0.06			8.1		Y
Aquila	J183329.4+024558	18:33:29.46	-02:45:58.32	1.65	1.03±0.10		7.47±0.04	0.79±0.08			10.4		Y
Aquila	J183602.6+000220	18:36:02.64	00:02:20.70	-1.59	<0.29						9.0		N
Aquila	J183623.7+001448	18:36:23.72	00:14:48.16	0.85	<0.81						7.9		N
Aquila	J183730.2+000706	18:37:30.22	00:07:06.48	0.33	0.52±0.12		9.42±0.08	0.78±0.24			13.4		N
Aquila	J183730.2+000711	18:37:30.28	00:07:11.00	0.20	0.64±0.11		9.46±0.07	0.90±0.21			13.4		N
Aquila	J183731.1+000706	18:37:31.16	00:07:06.19	0.43	<0.52						13.3		N
Aquila	J183739.2+002535	18:37:39.24	00:25:35.18	0.13	<0.20						8.1		N
Aquila	J183746.9+000155	18:37:46.90	00:01:55.83	0.76	<0.33						8.2		N
Aquila	J183855.7+002340	18:38:55.77	00:23:40.81	0.67	<0.31						11.8		N
Aquila	J183858.8+003309	18:38:58.89	00:33:09.10	2.11	4.48±0.24	1.62±0.20	8.07±0.04	1.58±0.11	9.47±0.03	0.77±0.08	22.2		Y
Aquila	J183901.3+003015	18:39:01.35	00:30:15.37	1.25	1.03±0.08		8.83±0.03	0.62±0.05			19.3		Y
Aquila	J183909.5+001354	18:39:09.53	00:13:54.78	0.12	1.75±0.14		9.52±0.02	0.68±0.07			11.9		Y
Aquila	J183909.7+003245	18:39:09.71	00:32:45.65	0.12	<0.57						23.4		N
Aquila	J183929.8+003740	18:39:29.87	00:37:40.47	0.25	<0.44						12.3		N
Aquila	J183931.5+000017	18:39:31.57	00:00:17.31	-0.49	<0.72						11.1		N
Aquila	J184012.0+002927	18:40:12.06	00:29:27.74	-0.49	<0.28						7.9		N
Aquila	J184017.6+001613	18:40:17.60	00:16:13.75	0.37	1.37±0.10		8.40±0.03	0.80±0.08			17.1		Y
Auriga North	J040124.5+410149	04:01:24.55	41:01:49.00	1.89	2.42±0.13		-6.94±0.05	1.88±0.11			7.4		Y
Auriga/CMC	J041002.6+400248	04:10:02.63	40:02:48.26	0.88	0.77±0.10		-4.74±0.05	0.88±0.15			8.9		Y
Auriga/CMC	J041008.4+400224	04:10:08.84	40:02:20.28	1.59	0.91±0.09		-4.47±0.06	1.09±0.12			8.9		Y
Auriga/CMC	J041011.1+400126	04:10:11.17	40:01:26.23	1.87	0.89±0.10		-4.69±0.05	0.86±0.11			8.6		Y
Auriga/CMC	J041944.6+381122	04:19:44.67	38:11:21.98	-0.26	0.09±0.02		3.09±0.03	0.20±0.67			6.7		N
Auriga/CMC	J042140.8+373359	04:21:40.80	37:33:59.08	1.84	1.77±0.15		-1.43±0.07	1.67±0.17			11.2		Y
Auriga/CMC	J042538.4+370701	04:25:38.49	37:07:01.22	1.30	0.48±0.08		-1.41±0.03	0.40±0.08			7.0		N
Auriga/CMC	J042539.7+370708	04:25:39.79	37:07:08.25	0.48	0.48±0.08		-2.17±0.04	0.47±0.08			7.2		N
Auriga/CMC	J042815.1+363028	04:28:15.15	36:30:28.67	0.23	<0.51						8.0		N
Auriga/CMC	J042835.0+362506	04:28:35.09	36:25:06.43	0.93	1.24±0.12		-1.84±0.06	1.20±0.14			6.7		Y
Auriga/CMC	J042838.5+362528	04:28:38.56	36:25:28.91	0.90	0.90±0.10		-1.41±0.05	0.94±0.13			6.9		Y
Auriga/CMC	J042843.6+362839	04:28:43.67	36:28:39.32	1.04	0.43±0.10		-1.19±0.12	1.02±0.25			8.0		N
Auriga/CMC	J042844.4+362445	04:28:44.43	36:24:45.67	-0.05	<0.37						6.2		N
Auriga/CMC	J042849.5+362910	04:28:49.58	36:29:10.73	0.34	<0.42						8.3		N
Auriga/CMC	J042855.3+363122	04:28:55.31	36:31:22.56	1.31	0.81±0.12		-1.39±0.04	0.68±0.15			8.1		Y
Auriga/CMC	J042940.0+352108	04:29:40.02	35:21:08.95	0.38	<0.26						8.3		N
Auriga/CMC	J042944.2+351230	04:29:44.21	35:12:30.09	-0.71	<0.47						9.6		N
Auriga/CMC	J042949.2+351422	04:29:49.22	35:14:22.72	-0.08	1.03±0.11		-0.42±0.04	0.72±0.08			11.1		Y
Auriga/CMC	J042951.0+351547	04:29:51.02	35:15:47.54	0.53	1.38±0.11		-0.51±0.03	0.70±0.07			11.8		Y
Auriga/CMC	J042953.4+351548	04:29:53.46	35:15:48.55	-0.74	1.58±0.14		-0.26±0.04	0.98±0.11			11.8		Y
Auriga/CMC	J042954.1+351021	04:29:54.15	35:10:21.69	-0.06	<0.57						8.1		N
Auriga/CMC	J042956.2+351742	04:29:56.27	35:17:42.93	0.63	<0.75						10.1		N
Auriga/CMC	J043003.6+351420	04:30:03.63	35:14:20.13	0.76	2.65±0.15		-0.56±0.03	1.02±0.07			12.0	N	Y
Auriga/CMC	J043008.2+351410	04:30:08.26	35:14:10.05	0.43	2.57±0.18		0.28±0.08	2.21±0.19			12.0	N	Y
Auriga/CMC	J043009.5+351440	04:30:09.52	35:14:40.33	0.31	1.20±0.12		0.40±0.10	2.22±0.28			11.7		Y
Auriga/CMC	J043014.9+360008	04:30:14.96	36:00:08.53	1.61	0.53±0.06		-0.93±0.04	0.66±0.09			8.1		N
Auriga/CMC	J043019.5+350821	04:30:19.59	35:08:21.68	-0.29	0.73±0.07		0.17±0.04	0.69±0.06			9.3		Y
Auriga/CMC	J043023.8+352112	04:30:23.83	35:21:12.35	0.46	<0.68						7.6		N
Auriga/CMC	J043024.6+354520	04:30:24.68	35:45:20.70	1.22	0.56±0.05		-1.39±0.06	1.34±0.15			8.9		N
Auriga/CMC	J043027.0+354550	04:30:27.05	35:45:50.56	-0.50	0.64±0.09		-1.65±0.05	0.75±0.13			9.4		N
Auriga/CMC	J043027.4+350917	04:30:27.41	35:09:17.84	1.60	3.78±0.14		0.86±0.04	2.38±0.10			9.5		Y
Auriga/CMC	J043027.7+354615	04:30:27.76	35:46:15.08	0.34	0.62±0.09		-1.34±0.08	0.93±0.13			9.4		N
Auriga/CMC	J043028.0+350916	04:30:28.09	35:09:16.48	1.29	3.78±0.11		0.90±0.03	2.19±0.08			9.5		Y
Auriga/CMC	J043028.4+354917	04:30:28.45	35:49:17.68	-0.84	1.02±0.10		-0.46±0.04	0.92±0.12			9.3		Y

Table 5 — Continued

Cloud Name (1)	Source Name (2)	RA _{obs} (J2000) (3)	DEC _{obs} (J2000) (4)	$\alpha_{E.C.}$ (5)	$\int T_{MB} dV$ (K km s ⁻¹) (6)	$\int T_{MB} dV$ (K km s ⁻¹) (7)	V (km s ⁻¹) (8)	ΔV (km s ⁻¹) (9)	V (km s ⁻¹) (10)	ΔV (km s ⁻¹) (11)	A_V (Mag) (12)	SMM (Y/N) (13)	Stg 0+I (Y/N) (14)
Auriga/CMC	J043031.5+354513	04:30:31.59	35:45:13.76	-0.25	1.32±0.12		-1.73±0.04	0.87±0.11			8.8		Y
Auriga/CMC	J043036.8+355436	04:30:36.81	35:54:36.29	1.33	6.51±0.12		-1.11±0.01	1.55±0.04			22.1		Y
Auriga/CMC	J043037.8+355101	04:30:37.89	35:51:01.45	1.17	2.01±0.11		-0.88±0.03	1.15±0.08			13.0		Y
Auriga/CMC	J043038.6+355439	04:30:38.65	35:54:39.16	0.12	2.03±0.14		-1.21±0.05	1.35±0.11			20.8		Y
Auriga/CMC	J043039.1+355203	04:30:39.17	35:52:03.80	-0.71	3.15±0.10		-1.09±0.02	1.13±0.04			14.5		Y
Auriga/CMC	J043039.3+355200	04:30:39.32	35:52:00.79	-0.69	3.32±0.12		-1.08±0.02	1.31±0.05			14.5		Y
Auriga/CMC	J043041.1+352941	04:30:41.17	35:29:41.08	1.34	0.74±0.05		4.69±0.02	0.55±0.04			7.2		Y
Auriga/CMC	J043044.2+355951	04:30:44.23	35:59:51.16	0.93	0.99±0.08		-1.30±0.04	0.99±0.08			8.7		Y
Auriga/CMC	J043046.2+345856	04:30:46.25	34:58:56.27	1.30	1.69±0.13		-0.65±0.05	1.32±0.12			8.1		Y
Auriga/CMC	J043048.5+353753	04:30:48.52	35:37:53.76	1.32	0.87±0.07		-0.81±0.04	0.87±0.08			7.2		Y
Auriga/CMC	J043048.6+345853	04:30:48.61	34:58:53.53	-0.66	2.64±0.14		-0.47±0.04	1.53±0.10			8.1		Y
Auriga/CMC	J043049.2+345610	04:30:49.23	34:56:10.32	0.40	<1.00						7.2		N
Auriga/CMC	J043053.5+345627	04:30:53.51	34:56:27.46	0.86	1.31±0.08		-0.73±0.02	0.74±0.06			7.0		Y
Auriga/CMC	J043055.9+345647	04:30:55.99	34:56:47.88	1.01	1.13±0.06		-0.64±0.02	0.61±0.04			7.0		Y
Auriga/CMC	J043056.6+353004	04:30:56.62	35:30:04.55	2.23	0.62±0.05		-1.25±0.02	0.51±0.05			7.0		N
Cepheus 4	J203943.0+670830	20:39:42.96	67:08:30.12	-0.30	<0.55						5.5		N
Cepheus 5	J205706.7+773656	20:57:06.75	77:36:56.11	0.17	1.11±0.14		-7.71±0.05	0.92±0.14			10.2		Y
Cepheus 5	J205707.9+773659	20:57:07.94	77:36:59.73	0.27	1.29±0.12		-7.82±0.06	1.22±0.13			10.2		Y
Cepheus 5	J205713.0+773543	20:57:12.99	77:35:43.76	-0.04	2.35±0.14		-8.19±0.03	1.09±0.08			9.9	Y	Y
Cepheus 3	J210020.7+681316	21:00:20.68	68:13:16.92	1.36	3.36±0.18		2.60±0.04	1.50±0.10			6.3	Y	Y
Cepheus 3	J210022.1+681258	21:00:22.13	68:12:58.55	0.53	2.50±0.13		2.52±0.03	1.12±0.07			5.5	Y	Y
Cepheus 3	J210132.8+681120	21:01:32.83	68:11:20.25	0.94	2.85±0.12		2.80±0.02	0.86±0.04			6.0	Y	Y
Cepheus 3	J210143.9+681403	21:01:43.89	68:14:03.31	0.34	<0.49						5.9		N
Cepheus 3	J210202.5+681158	21:02:02.45	68:11:58.73	-1.51	<0.54						8.1		N
Cepheus 3	J210214.1+680730	21:02:14.06	68:07:30.80	0.47	<0.61						5.8		N
Cepheus 3	J210221.2+675420	21:02:21.22	67:54:20.28	0.65	1.78±0.13		2.77±0.06	1.43±0.10			8.4	Y	Y
Cepheus 3	J210259.5+680632	21:02:59.46	68:06:32.24	0.29	<0.35						4.6		N
Cepheus 1	J222959.4+751403	22:29:59.42	75:14:03.70	0.17	0.52±0.09		-3.85±0.06	0.78±0.15			7.1	N	N
Cepheus 1	J223031.8+751409	22:30:31.79	75:14:09.38	0.64	1.39±0.10		-3.77±0.03	0.88±0.07			8.2	Y	Y
Cepheus 1	J223500.8+751536	22:35:00.82	75:15:36.42	-0.63	<1.20						6.1		N
Cepheus 1	J223514.1+751502	22:35:14.09	75:15:02.61	0.23	<0.74						6.0		N
Cepheus 1	J223605.6+751832	22:36:05.60	75:18:32.45	-0.19	0.51±0.09		-4.69±0.05	0.66±0.13			7.8		N
Cepheus 1	J223842.8+751136	22:38:42.77	75:11:36.70	0.90	4.47±0.20	4.14±0.20	-4.47±0.02	0.96±0.06	-2.91±0.02	0.96±0.06	12.2	Y	Y
Cepheus 1	J223846.9+751133	22:38:46.92	75:11:33.70	1.92	6.18±0.25	3.66±0.20	-4.34±0.02	1.19±0.06	-2.85±0.02	0.73±0.05	12.2	Y	Y
Cepheus 1	J223853.0+751123	22:38:52.99	75:11:23.54	0.46	3.65±0.16	1.77±0.12	-4.12±0.02	1.04±0.06	-2.91±0.02	0.55±0.04	10.8	Y	Y
Cepheus 1	J223913.3+751215	22:39:13.34	75:12:15.53	1.18	1.45±0.12	0.92±0.10	-4.37±0.04	0.91±0.10	-3.23±0.03	0.58±0.07	8.4		Y
Chamaeleon I	J110422.7-771808	11:04:22.73	-77:18:08.22	0.27	<0.56						4.1	N	N
Chamaeleon I	J110646.4-772232	11:06:46.49	-77:22:32.97	1.12	1.51±0.14	3.07±0.11	3.43±0.05	1.42±0.16	4.93±0.01	0.88±0.04	13.1	Y	Y
Chamaeleon I	J110658.0-772248	11:06:58.03	-77:22:48.87	0.91	0.28±0.04	1.14±0.06	3.95±0.02	0.39±0.05	4.99±0.02	0.85±0.05	11.8	N	Y
Chamaeleon I	J110709.2-772305	11:07:09.24	-77:23:05.02	0.69	0.26±0.04	0.68±0.06	4.00±0.03	0.36±0.07	5.01±0.02	0.56±0.06	12.1		N
Chamaeleon I	J110716.1-772306	11:07:16.19	-77:23:06.91	-0.04	0.11±0.03	0.50±0.06	4.11±0.01	0.17±0.37	5.03±0.07	1.24±0.20	12.1	N	N
Chamaeleon I	J110721.3-772211	11:07:21.37	-77:22:11.76	-0.45	<0.39						15.2	N	N
Chamaeleon I	J110757.9-773845	11:07:57.96	-77:38:45.20	-0.74	0.30±0.05		4.14±0.09	1.07±0.24			8.5		N
Chamaeleon I	J110802.9-773842	11:08:02.96	-77:38:42.87	-0.39	<0.40						8.5	N	N
Chamaeleon I	J110841.9-774327	11:08:41.99	-77:43:27.50	-0.35	0.20±0.06		4.10±0.11	0.71±0.26			8.0		N
Chamaeleon I	J110922.6-763432	11:09:22.62	-76:34:32.43	-0.52	<0.30						7.2		N
Chamaeleon I	J110928.5-763328	11:09:28.51	-76:33:28.41	1.29	<0.82						8.3	Y	N
Chamaeleon I	J110954.3-763111	11:09:54.35	-76:31:11.63	0.09	<0.57						5.6		N
Chamaeleon I	J110955.0-763241	11:09:55.03	-76:32:41.31	-0.35	<0.30						6.9		N
Chamaeleon I	J111003.3-763311	11:10:03.35	-76:33:11.35	-0.17	<0.28						7.3	N	N
Chamaeleon I	J111049.5-771751	11:10:49.54	-77:17:51.83	-1.16	<0.69						6.7		N
Chamaeleon I	J111110.7-764157	11:11:10.74	-76:41:57.49	-0.19	<0.25						4.9	N	N
Chamaeleon II	J125317.2-770710	12:53:17.23	-77:07:10.69	-0.65	1.59±0.09		3.03±0.03	1.03±0.06			10.6	N	Y
Chamaeleon II	J125342.8-771511	12:53:42.86	-77:15:11.45	0.33	<0.44						4.9	Y	N

Table 5 — *Continued*

Cloud Name (1)	Source Name (2)	RA _{obs} (J2000) (3)	DEC _{obs} (J2000) (4)	$\alpha_{E.C.}$ (5)	$\int T_{MB} dV$ (K km s ⁻¹) (6)	$\int T_{MB} dV$ (K km s ⁻¹) (7)	V (km s ⁻¹) (8)	ΔV (km s ⁻¹) (9)	V (km s ⁻¹) (10)	ΔV (km s ⁻¹) (11)	A_V (Mag) (12)	SMM (Y/N) (13)	Stg 0+I (Y/N) (14)
Chamaeleon II	J125906.5-770739	12:59:06.58	-77:07:39.92	1.10	0.51±0.05		2.84±0.02	0.47±0.05			11.8	Y	N
CrA	J185752.6-371440	18:57:52.63	-37:14:40.07	1.52	<0.43						1.6		N
CrA	J185943.9-370400	18:59:43.92	-37:04:00.11	-0.33	<0.61						4.9		N
CrA	J190015.5-365757	19:00:15.55	-36:57:57.71	0.29	<0.71						7.2		N
CrA	J190148.0-365722	19:01:48.03	-36:57:22.22	1.01	20.88±0.22		5.63±0.01	2.04±0.02			20.7	Y	Y
CrA	J190148.4-365714	19:01:48.46	-36:57:14.67	1.19	21.58±0.20		5.61±0.01	1.96±0.02			20.7	Y	Y
CrA	J190155.6-365651	19:01:55.60	-36:56:51.15	0.46	30.24±0.81		5.03±0.04	3.26±0.12			23.8		Y
CrA	J190256.8-370719	19:02:56.82	-37:07:19.36	0.00	1.48±0.11		5.90±0.02	0.48±0.05			13.6		Y
CrA	J190301.0-370753	19:03:01.03	-37:07:53.41	0.09	1.03±0.08		5.76±0.03	0.63±0.06			12.3		Y
CrA	J190355.2-370935	19:03:55.24	-37:09:35.92	0.23	<1.10						7.2		N
CrA	J190158.5-365708	19:01:58.54	-36:57:08.52	0.71	23.67±0.38		4.17±0.03	3.37±0.06			23.0	Y	Y
CrA	J190258.6-370735	19:02:58.67	-37:07:35.93	1.49	3.92±0.17		5.76±0.04	1.62±0.08			13.1	Y	Y
IC5146NW	J214443.0+474643	21:44:43.08	47:46:43.68	0.57	1.92±0.14		4.25±0.09	2.61±0.22			4.1		Y
IC5146NW	J214448.3+474459	21:44:48.31	47:44:59.64	1.85	0.66±0.12		4.38±0.17	1.92±0.46			4.5		N
IC5146NW	J214451.7+474044	21:44:51.79	47:40:44.76	1.01	3.67±0.17		4.03±0.05	1.96±0.11			6.2		Y
IC5146NW	J214452.0+474030	21:44:52.01	47:40:30.73	1.53	4.66±0.14		4.24±0.03	2.00±0.06			6.2		Y
IC5146NW	J214453.9+474543	21:44:53.98	47:45:43.56	0.45	0.74±0.11		5.07±0.09	1.15±0.19			4.3		Y
IC5146NW	J214457.0+474152	21:44:57.10	47:41:52.81	0.17	<0.63						5.9		N
IC5146NW	J214502.6+473307	21:45:02.64	47:33:07.56	1.12	0.78±0.09		3.91±0.04	0.65±0.09			4.4		Y
IC5146NW	J214508.3+473305	21:45:08.31	47:33:05.77	0.20	3.18±0.02		3.92±0.02	1.18±0.04			4.4		Y
IC5146NW	J214531.2+473621	21:45:31.22	47:36:21.24	0.56	0.38±0.09		3.82±0.09	0.71±0.20			5.9		N
IC5146NW	J214558.5+473601	21:45:58.59	47:36:01.08	1.10	0.90±0.06		3.85±0.05	1.51±0.11			6.9	Y	Y
IC5146NW	J214706.0+473939	21:47:06.02	47:39:39.24	0.40	0.34±0.06		4.32±0.05	0.51±0.11			4.8		N
IC5146NW	J214721.2+473226	21:47:21.19	47:32:26.16	0.27	2.61±0.22		4.09±0.07	1.95±0.22			8.7		Y
IC5146NW	J214722.6+473205	21:47:22.61	47:32:06.00	0.78	4.05±0.21		4.04±0.04	1.97±0.14			8.6		Y
IC5146NW	J214722.7+473214	21:47:22.78	47:32:14.99	0.61	6.98±0.20		4.07±0.04	3.25±0.11			8.7	Y	Y
IC5146NW	J214728.7+473217	21:47:28.80	47:32:17.52	0.07	0.61±0.13		3.75±0.10	0.91±0.28			8.4		N
IC5146NW	J214755.6+473711	21:47:55.68	47:37:11.28	0.92	0.53±0.07		4.81±0.06	0.93±0.17			5.7		N
IC5146NW	J214759.2+473626	21:47:59.25	47:36:26.64	1.15	0.73±0.09		5.17±0.04	0.73±0.14			5.2		Y
IC5146E	J215214.3+471454	21:52:14.36	47:14:54.60	0.45	<0.58						3.9		N
IC5146E	J215237.7+471438	21:52:37.78	47:14:38.40	0.58	1.55±0.10		6.24±0.03	0.89±0.06			5.0		Y
IC5146E	J215246.5+471249	21:52:46.58	47:12:49.32	-0.73	<0.87						4.8		N
IC5146E	J215306.9+471434	21:53:06.94	47:14:34.80	0.46	0.75±0.10		6.92±0.07	1.13±0.19			5.5		Y
IC5146E	J215325.0+471622	21:53:25.00	47:16:22.08	0.14	<0.46						6.7		N
IC5146E	J215328.3+471543	21:53:28.34	47:15:43.56	2.19	<0.35						6.9		N
IC5146E	J215328.6+471551	21:53:28.65	47:15:51.84	0.55	<0.85						6.9		N
IC5146E	J215330.4+471310	21:53:30.45	47:13:10.92	-0.30	<0.22						6.7		N
IC5146E	J215331.4+472217	21:53:31.49	47:22:17.39	1.41	0.47±0.07		8.56±0.04	0.48±0.08			5.2		N
IC5146E	J215333.1+471418	21:53:33.17	47:14:18.97	1.06	1.35±0.14		7.04±0.05	1.04±0.13			7.0		Y
IC5146E	J215333.9+471724	21:53:33.98	47:17:24.72	0.83	1.35±0.14		8.10±0.07	1.21±0.14			7.0		Y
IC5146E	J215336.2+471027	21:53:36.24	47:10:27.84	-0.31	<0.46						5.6		N
IC5146E	J215336.3+471903	21:53:36.34	47:19:04.08	1.93	1.97±0.10		8.07±0.02	0.97±0.05			6.5		Y
IC5146E	J215337.0+471817	21:53:37.08	47:18:17.27	0.47	1.12±0.11		8.17±0.06	1.17±0.12			6.8		Y
IC5146E	J215349.7+471351	21:53:49.78	47:13:51.24	0.46	1.26±0.11		7.82±0.05	1.12±0.12			7.2		Y
IC5146E	J215355.7+472030	21:53:55.70	47:20:30.13	1.54	<0.45						3.8		N
IC5146E	J215358.1+471445	21:53:58.18	47:14:45.59	0.86	<0.63						5.9		N
IC5146E	J215418.7+471209	21:54:18.76	47:12:09.73	-0.99	<0.28						3.4		N
Lupus I	J153848.3-344038	15:38:48.35	-34:40:38.24	0.28	<0.70						3.3		N
Lupus I	J154214.5-341025	15:42:14.58	-34:10:25.79	0.31	<0.52						3.8		N
Lupus I	J154302.2-344406	15:43:02.29	-34:44:06.22	0.17	<0.55						1.3		N
Lupus III	J160703.8-391111	16:07:03.85	-39:11:11.59	-0.18	<0.77						1.4		N
Lupus III	J160708.5-391407	16:07:08.57	-39:14:07.75	0.11	<0.47						1.8		N
Lupus III	J160754.7-391544	16:07:54.73	-39:15:44.49	-0.09	<0.34						2.1		N
Lupus III	J160829.7-390311	16:08:29.73	-39:03:11.01	0.63	<0.86						6.5		N

The Real Solar Neighborhood Protostars

Table 5 — Continued

Cloud Name (1)	Source Name (2)	RA _{obs} (J2000) (3)	DEC _{obs} (J2000) (4)	$\alpha_{E.C.}$ (5)	$\int T_{MB} dV$ (K km s ⁻¹) (6)	$\int T_{MB} dV$ (K km s ⁻¹) (7)	V (km s ⁻¹) (8)	ΔV (km s ⁻¹) (9)	V (km s ⁻¹) (10)	ΔV (km s ⁻¹) (11)	A_V (Mag) (12)	SMM (Y/N) (13)	Stg 0+I (Y/N) (14)
Lupus III	J160918.0-390453	16:09:18.07	-39:04:53.39	1.14	2.08±0.15		4.92±0.03	0.84±0.08			18.5	Y	Y
Lupus III	J161013.0-384616	16:10:13.06	-38:46:16.84	-0.50	<0.50						0.7		N
Lupus III	J161027.4-390230	16:10:27.43	-39:02:30.22	-0.21	<1.18						4.6		N
Lupus III	J161204.4-380959	16:12:04.48	-38:09:59.03	-0.06	<0.46						3.1		N
Lupus IV	J160221.6-414053	16:02:21.61	-41:40:53.70	0.45	<0.46						3.7		N
Lupus VI	J162451.7-395632	16:24:51.78	-39:56:32.66	0.71	<0.51						7.5		N
Musca	J121915.9-721825	12:19:15.94	-72:18:25.31	0.36	<0.33						2.0		N
Ophiuchus	J162138.7-225328	16:21:38.72	-22:53:28.26	0.85	<0.59						2.6		N
Ophiuchus	J162145.1-234231	16:21:45.13	-23:42:31.63	0.29	<0.45						9.7		N
Ophiuchus	J162220.9-230402	16:22:20.99	-23:04:02.35	0.23	<0.39						4.2		N
Ophiuchus	J162305.4-230256	16:23:05.43	-23:02:56.73	-0.23	<0.26						4.2		N
Ophiuchus	J162306.8-225736	16:23:06.86	-22:57:36.61	0.00	<0.34						4.8		N
Ophiuchus	J162332.2-242553	16:23:32.22	-24:25:53.82	-0.11	<0.33						3.8		N
Ophiuchus	J162340.0-233337	16:23:40.00	-23:33:37.36	-0.17	<0.37						4.3		N
Ophiuchus	J162527.5-243647	16:25:27.56	-24:36:47.55	0.07	<0.36						6.6		N
Ophiuchus	J162546.6-242336	16:25:46.63	-24:23:36.00	-0.21	<1.22						14.1		N
Ophiuchus	J162614.6-242507	16:26:14.63	-24:25:07.52	-999*	8.19±0.19		2.65±0.01	1.20±0.03			26.6	N	Y
Ophiuchus	J162617.2-242345	16:26:17.23	-24:23:45.15	0.70	7.95±0.17		2.58±0.01	0.94±0.02			30.5		Y
Ophiuchus	J162621.3-242304	16:26:21.35	-24:23:04.29	1.14	18.00±0.28		3.19±0.01	1.72±0.03			31.3	Y	Y
Ophiuchus	J162622.2-242407	16:26:22.25	-24:24:06.97	-0.15	6.97±0.15		2.74±0.01	1.28±0.03			30.6		Y
Ophiuchus	J162623.5-242439	16:26:23.57	-24:24:39.45	0.06	8.64±0.18		2.67±0.01	1.34±0.04			30.6		Y
Ophiuchus	J162625.4-242301	16:26:25.47	-24:23:01.30	0.61	18.61±0.24		3.38±0.01	1.92±0.03			29.8	N	Y
Ophiuchus	J162625.6-242428	16:26:25.62	-24:24:28.89	1.45	11.97±0.39	3.46±0.30	2.66±0.03	1.82±0.08	4.21±0.01	0.62±0.05	31.1	N	Y
Ophiuchus	J162625.9-242340	16:26:25.99	-24:23:40.46	-0.07	13.66±0.20		3.17±0.02	2.06±0.03			30.5		Y
Ophiuchus	J162626.4-242430	16:26:26.42	-24:24:29.98	-999*	15.12±0.19		3.32±0.02	2.61±0.04			31.1		Y
Ophiuchus	J162640.4-242714	16:26:40.46	-24:27:14.31	0.32	0.93±0.11		3.08±0.07	1.14±0.15			37.6	N	Y
Ophiuchus	J162644.1-243448	16:26:44.19	-24:34:48.36	2.50	1.26±0.10		4.25±0.03	0.83±0.07			24.0	N	Y
Ophiuchus	J162648.4-242838	16:26:48.47	-24:28:38.68	-0.06	0.45±0.12		3.62±0.11	0.79±0.28			37.2	N	N
Ophiuchus	J162653.4-243236	16:26:53.47	-24:32:36.13	-0.20	0.71±0.08		3.73±0.06	1.00±0.12			33.6		Y
Ophiuchus	J162654.2-242437	16:26:54.28	-24:24:37.89	-0.21	0.65±0.09		3.53±0.06	0.87±0.14			30.1		N
Ophiuchus	J162658.2-243740	16:26:58.27	-24:37:40.75	-0.33	0.66±0.06		4.64±0.03	0.70±0.09			27.2		N
Ophiuchus	J162702.3-243727	16:27:02.32	-24:37:27.18	0.92	<0.52						30.4	N	N
Ophiuchus	J162702.9-242614	16:27:02.99	-24:26:14.61	-0.23	0.78±0.06		3.31±0.02	0.48±0.04			30.2	N	Y
Ophiuchus	J162704.1-242829	16:27:04.10	-24:28:29.86	-0.22	0.66±0.10		3.28±0.08	1.21±0.23			37.1		N
Ophiuchus	J162705.2-243629	16:27:05.24	-24:36:29.59	1.08	2.35±0.14		4.60±0.03	0.90±0.06			32.1	N	Y
Ophiuchus	J162706.7-243814	16:27:06.75	-24:38:14.84	0.72	0.93±0.07		4.61±0.03	0.93±0.08			31.1	N	Y
Ophiuchus	J162709.4-243718	16:27:09.40	-24:37:18.61	1.06	2.62±0.23		4.77±0.06	1.68±0.20			32.6	N	Y
Ophiuchus	J162711.1-244046	16:27:11.17	-24:40:46.55	-0.11	0.35±0.05		4.23±0.06	0.68±0.12			26.0		N
Ophiuchus	J162714.4-242645	16:27:14.49	-24:26:45.88	-0.01	2.06±0.16		4.15±0.03	0.92±0.10			33.4		Y
Ophiuchus	J162715.5-243053	16:27:15.50	-24:30:53.65	-0.02	2.72±0.10		3.74±0.02	1.10±0.04			35.4		Y
Ophiuchus	J162715.8-242513	16:27:15.87	-24:25:13.93	-0.21	1.50±0.13		3.45±0.03	0.65±0.07			30.5		Y
Ophiuchus	J162716.3-243114	16:27:16.39	-24:31:14.47	0.04	2.54±0.13		3.66±0.03	1.23±0.06			34.5		Y
Ophiuchus	J162717.5-242856	16:27:17.58	-24:28:56.21	0.36	4.70±0.20		4.16±0.04	2.16±0.10			35.2	N	Y
Ophiuchus	J162718.3-243914	16:27:18.37	-24:39:14.56	0.20	1.21±0.13		4.32±0.04	0.82±0.10			31.2		Y
Ophiuchus	J162719.2-242843	16:27:19.20	-24:28:43.78	0.07	4.81±0.19		4.20±0.03	1.74±0.08			35.2		Y
Ophiuchus	J162721.4-244143	16:27:21.45	-24:41:42.95	-0.03	0.92±0.13		4.20±0.11	1.34±0.26			31.3	N	Y
Ophiuchus	J162721.7-242953	16:27:21.79	-24:29:53.13	1.00	1.18±0.09		3.98±0.07	1.95±0.20			33.2		Y
Ophiuchus	J162721.8-242727	16:27:21.83	-24:27:27.56	-0.07	5.64±0.18		4.00±0.03	1.55±0.05			33.8	N	Y
Ophiuchus	J162724.5-244103	16:27:24.58	-24:41:03.09	1.23	4.06±0.19		4.27±0.05	2.30±0.12			31.3	N	Y
Ophiuchus	J162726.2-244246	16:27:26.27	-24:42:46.08	-0.13	<0.77						30.7		N
Ophiuchus	J162726.9-244050	16:27:26.91	-24:40:50.66	1.15	3.16±0.19		3.88±0.08	2.73±0.20			29.5	N	Y
Ophiuchus	J162727.9-243933	16:27:27.99	-24:39:33.36	2.11	3.88±0.20		3.64±0.13	5.29±0.31			24.9	N	Y
Ophiuchus	J162728.4-242721	16:27:28.44	-24:27:20.97	-0.14	3.07±0.26	5.55±0.25	3.42±0.04	0.89±0.09	4.57±0.01	0.77±0.04	29.4	N	Y
Ophiuchus	J162730.1-242743	16:27:30.17	-24:27:43.21	-0.03	1.49±0.15	4.96±0.16	3.24±0.04	0.88±0.10	4.57±0.00	0.95±0.04	29.4	N	Y

Table 5 — *Continued*

Cloud Name (1)	Source Name (2)	RA _{obs} (J2000) (3)	DEC _{obs} (J2000) (4)	$\alpha_{E.C.}$ (5)	$\int T_{MB} dV$ (K km s ⁻¹) (6)	$\int T_{MB} dV$ (K km s ⁻¹) (7)	V (km s ⁻¹) (8)	ΔV (km s ⁻¹) (9)	V (km s ⁻¹) (10)	ΔV (km s ⁻¹) (11)	A_V (Mag) (12)	SMM (Y/N) (13)	Stg 0+I (Y/N) (14)
Ophiuchus	J162730.9-242733	16:27:30.91	-24:27:33.17	0.67	6.15±0.21		4.47±0.03	1.56±0.08			26.6		Y
Ophiuchus	J162737.2-244237	16:27:37.23	-24:42:37.86	0.14	1.82±0.13		3.83±0.05	1.20±0.09			25.9	N	Y
Ophiuchus	J162738.9-244020	16:27:38.93	-24:40:20.47	0.25	<0.42						20.5		N
Ophiuchus	J162739.8-244315	16:27:39.81	-24:43:15.00	-0.15	0.86±0.09		3.85±0.04	0.71±0.08			26.2	N	Y
Ophiuchus	J162741.6-244644	16:27:41.60	-24:46:44.62	0.17	<0.71						16.9		N
Ophiuchus	J162741.7-244336	16:27:41.74	-24:43:35.99	-0.27	0.74±0.10		3.70±0.05	0.71±0.09			24.7		Y
Ophiuchus	J162745.7-244453	16:27:45.77	-24:44:53.82	0.13	1.27±0.11		3.68±0.04	0.79±0.07			21.3		Y
Ophiuchus	J162748.2-244225	16:27:48.23	-24:42:25.44	1.10	0.86±0.09		3.74±0.03	0.61±0.08			21.0		Y
Ophiuchus	J162751.7-243145	16:27:51.79	-24:31:45.41	-0.20	0.79±0.11		4.21±0.05	0.69±0.13			17.7		Y
Ophiuchus	J162821.6-243623	16:28:21.61	-24:36:23.41	0.97	2.56±0.10		4.06±0.02	0.81±0.03			19.1	Y	Y
Ophiuchus	J162857.8-244054	16:28:57.85	-24:40:54.87	0.57	0.22±0.06		3.62±0.06	0.44±0.11			10.4	N	N
Ophiuchus	J163041.4-241320	16:30:41.47	-24:13:20.59	-0.72	<0.55						0.9		N
Ophiuchus	J163129.2-240431	16:31:29.23	-24:04:31.10	-0.23	<0.53						4.9		N
Ophiuchus	J163131.2-242627	16:31:31.24	-24:26:27.87	-0.63	<0.70						2.5		N
Ophiuchus	J163134.2-240325	16:31:34.28	-24:03:25.18	-0.04	<0.92						9.3		N
Ophiuchus	J163135.6-240129	16:31:35.65	-24:01:29.33	0.13	1.08±0.12		2.87±0.05	0.79±0.09			17.3	Y	Y
Ophiuchus	J163143.7-245524	16:31:43.75	-24:55:24.61	0.18	2.28±0.14		4.83±0.03	1.14±0.08			15.0	N	Y
Ophiuchus	J163152.0-245726	16:31:52.06	-24:57:26.02	0.61	1.38±0.12		4.45±0.05	1.10±0.11			19.7	N	Y
Ophiuchus	J163152.4-245536	16:31:52.45	-24:55:36.18	0.86	4.25±0.14		4.70±0.02	1.18±0.05			17.5	N	Y
Ophiuchus	J163200.9-245642	16:32:00.99	-24:56:42.60	1.37	5.57±0.22		4.05±0.05	2.41±0.12			18.9	Y	Y
Ophiuchus	J163222.6-242831	16:32:22.62	-24:28:31.81	4.89	26.66±2.06		3.14±0.04	1.16±0.12			25.0	Y	Y
Ophiuchus	J164424.2-240124	16:44:24.27	-24:01:24.56	0.30	<0.56						2.8		N
Ophiuchus	J164526.6-240305	16:45:26.65	-24:03:05.41	0.23	<0.50						2.8		N
Perseus	J032519.5+303424	03:25:19.52	30:34:24.16	-0.14	<0.32						2.3		N
Perseus	J032522.3+304513	03:25:22.32	30:45:13.92	2.21	3.63±0.14		4.06±0.01	1.61±0.07			18.0	Y	Y
Perseus	J032536.2+304515	03:25:36.22	30:45:15.71	1.51	11.52±0.19		4.71±0.02	2.21±0.04			11.2	Y	Y
Perseus	J032536.4+304522	03:25:36.49	30:45:22.15	2.56	12.68±0.19		4.86±0.02	2.11±0.04			11.2	Y	Y
Perseus	J032538.8+304406	03:25:38.83	30:44:06.19	2.05	1.92±0.16	4.65±0.16	4.11±0.03	0.73±0.09	5.48±0.01	0.93±0.04	9.3	Y	Y
Perseus	J032539.1+304358	03:25:39.12	30:43:58.16	2.00	2.12±0.10	4.35±0.11	4.15±0.02	0.75±0.05	5.63±0.01	0.93±0.03	9.0	N	Y
Perseus	J032637.4+301528	03:26:37.47	30:15:28.08	1.03	0.47±0.08		5.33±0.10	0.99±0.19			2.6	Y	N
Perseus	J032739.0+301303	03:27:39.08	30:13:03.15	2.46	5.18±0.19		4.62±0.03	1.60±0.07			9.3	Y	Y
Perseus	J032743.2+301228	03:27:43.23	30:12:28.90	2.23	3.23±0.13		4.77±0.02	1.01±0.05			9.1	Y	Y
Perseus	J032747.6+301204	03:27:47.67	30:12:04.53	-0.25	3.09±0.10		5.08±0.02	1.18±0.05			9.3	Y	Y
Perseus	J032800.3+300801	03:28:00.39	30:08:01.26	0.98	0.73±0.09		4.83±0.05	0.81±0.13			9.7	Y	Y
Perseus	J032832.5+311105	03:28:32.56	31:11:05.15	0.51	1.97±0.12		6.73±0.04	1.31±0.10			13.1	Y	Y
Perseus	J032834.4+310051	03:28:34.49	31:00:51.10	0.88	0.25±0.03		9.19±0.02	0.34±0.04			5.8	Y	N
Perseus	J032834.5+310705	03:28:34.53	31:07:05.50	0.31	0.85±0.08		6.81±0.03	0.74±0.08			7.2	Y	Y
Perseus	J032834.9+305454	03:28:34.94	30:54:54.55	-0.06	<0.45						3.3		N
Perseus	J032835.0+302009	03:28:35.03	30:20:09.87	-0.20	<0.43						10.3	Y	N
Perseus	J032837.0+311330	03:28:37.09	31:13:30.84	1.93	3.45±0.12		7.11±0.02	0.97±0.04			17.8	Y	Y
Perseus	J032838.7+311806	03:28:38.78	31:18:06.58	-0.25	2.42±0.12		7.93±0.04	1.56±0.09			14.8		Y
Perseus	J032839.1+310601	03:28:39.10	31:06:01.72	1.55	1.97±0.11		6.91±0.02	0.73±0.05			7.5	Y	Y
Perseus	J032840.6+311756	03:28:40.63	31:17:56.47	0.96	3.03±0.16		7.95±0.04	1.49±0.08			15.7	Y	Y
Perseus	J032843.2+311732	03:28:43.28	31:17:32.92	0.24	1.14±0.10		8.09±0.04	0.96±0.09			16.3	Y	Y
Perseus	J032845.3+310541	03:28:45.30	31:05:41.92	1.09	1.58±0.14		7.18±0.03	0.74±0.09			6.6	Y	Y
Perseus	J032848.7+311608	03:28:48.77	31:16:08.75	0.20	2.48±0.17		8.02±0.04	1.30±0.11			19.4		Y
Perseus	J032851.2+311739	03:28:51.26	31:17:39.32	0.60	4.15±0.12		7.56±0.02	1.50±0.05			16.5		Y
Perseus	J032855.5+311436	03:28:55.55	31:14:36.74	2.39	8.27±0.23		7.43±0.04	2.87±0.10			19.7	Y	Y
Perseus	J032856.6+310737	03:28:56.60	31:07:36.96	0.01	<0.39						6.9		N
Perseus	J032857.3+311415	03:28:57.36	31:14:15.86	1.40	6.63±0.15		7.07±0.02	1.63±0.05			19.7	Y	Y
Perseus	J032858.2+312209	03:28:58.26	31:22:09.22	-0.99	4.76±0.15		7.93±0.02	1.58±0.05			16.7		Y
Perseus	J032858.4+312217	03:28:58.43	31:22:17.53	0.82	4.62±0.15		7.85±0.03	1.58±0.06			16.7	Y	Y
Perseus	J032859.2+312032	03:28:59.23	31:20:32.49	-0.02	15.12±0.17		7.97±0.01	1.73±0.02			15.7		Y
Perseus	J032859.3+311548	03:28:59.32	31:15:48.67	-0.08	4.56±0.17		7.92±0.03	1.79±0.08			17.4	Y	Y

Table 5 — Continued

Cloud Name (1)	Source Name (2)	RA _{obs} (J2000) (3)	DEC _{obs} (J2000) (4)	$\alpha_{E.C.}$ (5)	$\int T_{MB} dV$ (K km s ⁻¹) (6)	$\int T_{MB} dV$ (K km s ⁻¹) (7)	V (km s ⁻¹) (8)	ΔV (km s ⁻¹) (9)	V (km s ⁻¹) (10)	ΔV (km s ⁻¹) (11)	A_V (Mag) (12)	SMM (Y/N) (13)	Stg 0+I (Y/N) (14)
Perseus	J032900.5+311200	03:29:00.55	31:12:00.80	1.96	4.01±0.12		7.10±0.01	1.04±0.04			14.0	Y	Y
Perseus	J032901.5+312020	03:29:01.56	31:20:20.61	2.30	9.94±0.15		7.91±0.01	1.86±0.04			15.6	Y	Y
Perseus	J032901.8+311653	03:29:01.88	31:16:53.17	-0.15	1.33±0.12		8.26±0.08	1.71±0.18			15.8		Y
Perseus	J032903.3+312314	03:29:03.33	31:23:14.61	1.00	0.74±0.06		7.59±0.07	1.57±0.17			17.0	N	Y
Perseus	J032903.7+311603	03:29:03.78	31:16:03.83	0.85	11.84±0.16		8.35±0.01	1.61±0.03			16.7	Y	Y
Perseus	J032904.0+311446	03:29:04.06	31:14:46.54	1.32	8.12±0.19		6.97±0.03	2.25±0.06			17.4	Y	Y
Perseus	J032904.6+312205	03:29:04.64	31:22:05.72	-999*	4.00±0.13		7.40±0.02	1.28±0.05			16.4		Y
Perseus	J032904.9+312038	03:29:04.95	31:20:38.36	0.06	6.43±0.24		7.61±0.03	1.43±0.06			15.1		Y
Perseus	J032906.0+303039	03:29:06.05	30:30:39.19	0.64	<0.24						1.8		N
Perseus	J032907.7+312157	03:29:07.78	31:21:57.25	2.30	5.26±0.20		7.50±0.03	1.51±0.07			15.6	Y	Y
Perseus	J032909.1+312128	03:29:09.10	31:21:28.75	1.05	6.25±0.13		7.47±0.01	0.98±0.02			14.2		Y
Perseus	J032910.4+311331	03:29:10.49	31:13:30.98	2.49	9.46±0.28		6.53±0.02	1.29±0.05			13.1	Y	Y
Perseus	J032910.6+311340	03:29:10.65	31:13:40.03	0.42	10.23±0.55		6.76±0.05	2.04±0.20			13.1		Y
Perseus	J032910.6+311820	03:29:10.68	31:18:20.61	1.84	6.53±0.17		8.48±0.02	1.68±0.05			14.8	Y	Y
Perseus	J032910.9+311826	03:29:10.99	31:18:26.01	0.60	7.60±0.19		8.44±0.02	1.72±0.05			14.8		Y
Perseus	J032911.2+311831	03:29:11.26	31:18:31.45	1.79	7.73±0.20		8.36±0.02	1.73±0.05			14.8	Y	Y
Perseus	J032911.8+312127	03:29:11.89	31:21:26.98	0.32	5.23±0.19		7.51±0.02	1.07±0.05			12.9		Y
Perseus	J032912.0+311301	03:29:12.06	31:13:01.72	0.07	5.46±0.34		6.51±0.03	1.20±0.11			11.0		Y
Perseus	J032912.9+311814	03:29:12.97	31:18:14.31	1.56	5.54±0.17		8.53±0.02	1.58±0.05			14.3	N	Y
Perseus	J032913.5+311358	03:29:13.54	31:13:58.17	2.50	3.77±0.17		7.94±0.03	1.52±0.08			11.5	Y	Y
Perseus	J032917.1+312746	03:29:17.17	31:27:46.47	1.69	3.36±0.12		7.43±0.01	0.87±0.03			8.9	Y	Y
Perseus	J032917.5+312748	03:29:17.50	31:27:48.32	0.89	3.37±0.11		7.39±0.01	0.91±0.04			8.9		Y
Perseus	J032918.2+312319	03:29:18.26	31:23:19.87	1.09	2.06±0.11		7.63±0.02	0.73±0.05			11.2	Y	Y
Perseus	J032918.6+312017	03:29:18.67	31:20:17.73	0.16	1.81±0.11		8.53±0.04	1.30±0.09			12.0		Y
Perseus	J032920.0+312407	03:29:20.06	31:24:07.53	0.34	2.95±0.18		7.51±0.03	1.00±0.07			9.7	Y	Y
Perseus	J032920.4+311834	03:29:20.44	31:18:34.21	-0.25	0.60±0.09		8.41±0.07	1.18±0.26			11.9		N
Perseus	J032923.4+313329	03:29:23.48	31:33:29.54	1.53	1.91±0.10		7.49±0.02	0.73±0.05			10.3	Y	Y
Perseus	J032924.0+311957	03:29:24.09	31:19:57.63	-0.13	<0.41						9.7		N
Perseus	J032951.8+313906	03:29:51.82	31:39:06.03	3.40	1.87±0.08		4.00±0.01	0.57±0.03			6.1	Y	Y
Perseus	J033015.1+302349	03:30:15.14	30:23:49.38	1.58	1.49±0.11		5.90±0.03	0.82±0.09			12.3	Y	Y
Perseus	J033022.4+313240	03:30:22.45	31:32:40.53	0.28	<0.41						3.0		N
Perseus	J033027.1+302829	03:30:27.14	30:28:29.76	-0.16	<0.30						7.4		N
Perseus	J033032.6+302626	03:30:32.68	30:26:26.57	2.66	1.31±0.10		6.00±0.04	0.96±0.08			8.9	Y	Y
Perseus	J033038.2+303211	03:30:38.21	30:32:11.93	-0.02	<0.46						4.5		N
Perseus	J033114.7+304955	03:31:14.70	30:49:55.40	-0.07	<0.27						1.9		N
Perseus	J033120.9+304530	03:31:20.98	30:45:30.06	1.48	3.60±0.08		6.87±0.01	1.06±0.03			4.4	Y	Y
Perseus	J033217.9+304947	03:32:17.96	30:49:47.50	0.86	3.86±0.15		6.84±0.03	1.23±0.05			7.9	Y	Y
Perseus	J033229.1+310240	03:32:29.17	31:02:40.85	0.16	0.57±0.09		6.64±0.05	0.57±0.12			11.6	Y	N
Perseus	J033257.8+310608	03:32:57.84	31:06:08.25	0.33	0.32±0.09		6.50±0.12	0.73±0.18			16.3		N
Perseus	J033306.4+310804	03:33:06.41	31:08:04.56	0.17	0.29±0.08		6.43±0.07	0.52±0.14			16.4		N
Perseus	J033309.5+310531	03:33:09.56	31:05:31.18	0.70	0.95±0.08		6.67±0.05	1.25±0.11			18.8	N	Y
Perseus	J033312.8+312124	03:33:12.84	31:21:24.24	0.16	0.35±0.07		7.08±0.04	0.37±0.08			11.1	Y	N
Perseus	J033313.8+312005	03:33:13.80	31:20:05.29	1.31	0.47±0.12		7.21±0.13	1.07±0.29			13.3	Y	N
Perseus	J033314.3+310710	03:33:14.38	31:07:10.88	2.72	2.62±0.19		5.82±0.02	0.87±0.10			20.7	Y	Y
Perseus	J033316.4+310652	03:33:16.44	31:06:52.54	1.56	2.15±0.16		5.95±0.03	0.71±0.07			21.0	Y	Y
Perseus	J033316.6+310755	03:33:16.65	31:07:55.16	1.69	3.91±0.21		5.91±0.03	1.14±0.08			21.2	Y	Y
Perseus	J033317.8+310931	03:33:17.85	31:09:31.92	2.90	5.81±0.16		5.73±0.02	1.32±0.05			17.1	Y	Y
Perseus	J033320.3+310721	03:33:20.31	31:07:21.48	0.61	4.10±0.14		6.28±0.02	1.31±0.06			20.8	Y	Y
Perseus	J033327.2+310710	03:33:27.29	31:07:10.22	1.82	1.54±0.10		6.95±0.04	1.05±0.08			18.9	Y	Y
Perseus	J034141.0+314804	03:41:41.09	31:48:04.64	-0.16	<0.98						11.7		N
Perseus	J034155.7+314811	03:41:55.71	31:48:11.43	0.28	<0.39						11.8		N
Perseus	J034158.6+314821	03:41:58.67	31:48:21.43	0.47	<0.38						11.8		N
Perseus	J034202.1+314802	03:42:02.17	31:48:02.05	1.23	<0.66						12.3	N	N
Perseus	J034256.0+315644	03:42:56.05	31:56:44.81	0.06	<1.60						12.5		N

Table 5 — Continued

Cloud Name (1)	Source Name (2)	RA _{obs} (J2000) (3)	DEC _{obs} (J2000) (4)	$\alpha_{E.C.}$ (5)	$\int T_{MB} dV$ (K km s ⁻¹) (6)	$\int T_{MB} dV$ (K km s ⁻¹) (7)	V (km s ⁻¹) (8)	ΔV (km s ⁻¹) (9)	V (km s ⁻¹) (10)	ΔV (km s ⁻¹) (11)	A_V (Mag) (12)	SMM (Y/N) (13)	Stg 0+I (Y/N) (14)
Perseus	J034329.4+315219	03:43:29.44	31:52:19.45	0.41	<0.50						11.9		N
Perseus	J034336.0+315009	03:43:36.02	31:50:08.99	-0.18	<0.34						10.0		N
Perseus	J034345.1+320358	03:43:45.17	32:03:58.62	0.11	1.22±0.17		8.62±0.11	1.63±0.32			13.7	N	Y
Perseus	J034350.9+320324	03:43:50.96	32:03:24.72	1.39	4.22±0.11		8.46±0.01	1.05±0.03			15.9	Y	Y
Perseus	J034351.0+320308	03:43:51.02	32:03:08.10	-0.29	5.02±0.18		8.56±0.02	1.11±0.05			15.9	Y	Y
Perseus	J034356.5+320052	03:43:56.52	32:00:52.82	0.57	4.21±0.16		9.02±0.03	1.43±0.06			18.1	Y	Y
Perseus	J034356.8+320304	03:43:56.84	32:03:04.74	1.83	4.32±0.14		8.61±0.02	1.05±0.04			15.9	Y	Y
Perseus	J034357.2+320047	03:43:57.27	32:00:47.47	-0.07	2.44±0.15		8.65±0.07	2.29±0.16			18.3		Y
Perseus	J034357.8+320312	03:43:57.82	32:03:12.36	1.75	3.66±0.13		8.63±0.02	1.10±0.05			15.7		Y
Perseus	J034359.4+320035	03:43:59.41	32:00:35.65	-0.18	3.89±0.16		8.78±0.06	1.54±0.16			18.3		Y
Perseus	J034402.4+320204	03:44:02.40	32:02:04.91	1.47	5.40±0.13		9.09±0.01	1.20±0.03			16.9	Y	Y
Perseus	J034402.6+320159	03:44:02.63	32:01:59.53	0.92	5.29±0.14		9.05±0.02	1.34±0.04			18.0		Y
Perseus	J034409.2+320237	03:44:09.20	32:02:37.82	0.61	<1.18						14.4		N
Perseus	J034412.9+320135	03:44:12.98	32:01:35.48	0.29	<0.54						14.8	N	N
Perseus	J034421.3+315932	03:44:21.35	31:59:32.58	0.52	1.19±0.14		9.05±0.05	0.79±0.10			18.0	Y	Y
Perseus	J034424.8+321348	03:44:24.84	32:13:48.36	1.65	<0.70						6.3		N
Perseus	J034430.3+321135	03:44:30.30	32:11:35.17	0.05	<0.46						7.2		N
Perseus	J034435.3+322837	03:44:35.34	32:28:37.18	-0.16	<0.27						2.7		N
Perseus	J034443.3+320131	03:44:43.32	32:01:31.53	0.61	4.94±0.17		9.90±0.03	1.88±0.08			11.2	N	Y
Perseus	J034443.9+320136	03:44:43.96	32:01:36.16	0.74	4.53±0.19		9.81±0.04	1.79±0.10			11.2	Y	Y
Perseus	J034513.8+321210	03:45:13.82	32:12:10.00	0.43	<0.20						2.9		N
Perseus	J034705.4+324308	03:47:05.43	32:43:08.53	0.51	1.19±0.05		10.86±0.01	0.63±0.03			4.8	Y	Y
Perseus	J034741.5+325144	03:47:41.58	32:51:44.06	1.30	1.68±0.10		10.29±0.02	0.65±0.05			8.9	Y	Y
Scorpius/OphN	J164658.2-093519	16:46:58.27	-09:35:19.76	0.61	<1.13						13.2	Y	N
Scorpius/OphN	J162204.3-194326	16:22:04.35	-19:43:26.76	-0.01	<0.82						5.9		N
Serpens	J182815.0+000258	18:28:15.02	00:02:58.80	-0.48	<0.46						7.0		N
Serpens	J182841.8+000321	18:28:41.87	00:03:21.34	0.18	<0.45						9.3		N
Serpens	J182844.0+005337	18:28:44.01	00:53:37.93	0.34	0.36±0.06		7.99±0.07	0.79±0.15			7.0	N	N
Serpens	J182844.7+005125	18:28:44.78	00:51:25.79	0.84	1.26±0.11		7.75±0.05	1.11±0.09			7.5	N	Y
Serpens	J182844.9+005203	18:28:44.96	00:52:03.54	1.12	1.98±0.17		7.80±0.05	1.14±0.12			7.5	Y	Y
Serpens	J182851.2+001927	18:28:51.23	00:19:27.31	0.29	0.58±0.06		8.02±0.04	0.62±0.08			15.5	N	N
Serpens	J182852.7+002846	18:28:52.76	00:28:46.79	-0.15	2.04±0.09	0.88±0.07	7.64±0.02	1.07±0.07	9.02±0.02	0.59±0.06	17.5		Y
Serpens	J182854.0+002930	18:28:54.05	00:29:29.99	1.15	3.17±0.22	2.27±0.25	7.23±0.03	1.16±0.07	8.97±0.08	1.66±0.22	19.3	Y	Y
Serpens	J182854.8+002952	18:28:54.87	00:29:52.51	1.60	2.17±0.10	2.55±0.10	7.14±0.02	1.03±0.06	8.67±0.02	0.88±0.04	20.2	Y	Y
Serpens	J182855.7+002944	18:28:55.77	00:29:44.78	1.65	2.52±0.15	2.71±0.16	7.15±0.03	1.03±0.07	8.73±0.03	1.02±0.08	19.6	Y	Y
Serpens	J182856.6+003008	18:28:56.65	00:30:08.25	1.61	2.74±0.24	1.68±0.22	7.41±0.04	1.06±0.11	8.48±0.04	0.72±0.09	19.6		Y
Serpens	J182902.1+003120	18:29:02.12	00:31:20.65	0.19	1.77±0.13		8.15±0.06	1.70±0.13			19.2	N	Y
Serpens	J182904.3+003324	18:29:04.37	00:33:24.01	0.54	<0.63						16.5		N
Serpens	J182906.2+003043	18:29:06.20	00:30:43.28	1.33	2.99±0.14	3.53±0.16	7.04±0.02	0.93±0.05	8.69±0.02	1.16±0.07	17.1	Y	Y
Serpens	J182906.7+003034	18:29:06.76	00:30:34.33	1.40	3.12±0.14	3.62±0.16	7.06±0.02	0.81±0.05	8.57±0.03	1.19±0.06	17.1	N	Y
Serpens	J182909.0+003128	18:29:09.05	00:31:28.02	0.07	3.90±0.22		8.28±0.08	2.92±0.20			16.8		Y
Serpens	J182909.0+003132	18:29:09.07	00:31:32.39	2.13	3.90±0.21		8.23±0.07	2.83±0.20			16.8	Y	Y
Serpens	J182916.1+001822	18:29:16.18	00:18:22.71	0.06	1.72±0.13		8.92±0.05	1.40±0.13			6.2	Y	Y
Serpens	J182927.3+003849	18:29:27.35	00:38:49.75	0.11	<0.30						13.5		N
Serpens	J182931.9+011842	18:29:31.96	01:18:42.92	-0.06	1.37±0.05		9.04±0.01	0.77±0.03			12.2	Y	Y
Serpens	J182940.2+001513	18:29:40.20	00:15:13.11	0.62	<0.31						5.1		N
Serpens	J182947.0+011626	18:29:47.01	01:16:26.90	-0.05	5.40±0.18	3.94±0.18	9.65±0.02	1.21±0.05	7.54±0.03	1.34±0.08	20.8		Y
Serpens	J182948.1+011644	18:29:48.11	01:16:44.92	1.11	8.15±0.16	7.95±0.11	7.03±0.02	2.35±0.06	9.61±0.01	1.12±0.02	20.8	Y	Y
Serpens	J182949.1+011619	18:29:49.13	01:16:19.86	3.48	2.90±0.17	5.27±0.17	7.65±0.02	0.94±0.06	9.52±0.03	1.92±0.10	20.8	N	Y
Serpens	J182949.6+011456	18:29:49.69	01:14:56.82	-0.04	5.35±0.33	2.61±0.32	7.58±0.05	1.96±0.15	10.01±0.08	1.66±0.24	20.4		Y
Serpens	J182952.0+003643	18:29:52.06	00:36:43.64	-0.14	0.68±0.14		10.08±0.11	1.01±0.29			13.7		N
Serpens	J182953.0+003606	18:29:53.05	00:36:06.72	-0.35	2.16±0.16		9.96±0.05	1.50±0.13			12.9		Y
Serpens	J182954.3+003601	18:29:54.31	00:36:01.31	-0.33	1.89±0.17		10.07±0.07	1.55±0.17			12.9	Y	Y
Serpens	J182956.6+011239	18:29:56.67	01:12:39.21	0.37	7.24±0.23		7.96±0.04	2.70±0.11			17.6		Y

Table 5 — Continued

Cloud Name (1)	Source Name (2)	RA _{obs} (J2000) (3)	DEC _{obs} (J2000) (4)	$\alpha_{E.C.}$ (5)	$\int T_{MB} dV$ (K km s ⁻¹) (6)	$\int T_{MB} dV$ (K km s ⁻¹) (7)	V (km s ⁻¹) (8)	ΔV (km s ⁻¹) (9)	V (km s ⁻¹) (10)	ΔV (km s ⁻¹) (11)	A_V (Mag) (12)	SMM (Y/N) (13)	Stg 0+I (Y/N) (14)
Serpens	J182956.8+011446	18:29:56.87	01:14:46.50	0.32	5.20±0.21		8.21±0.04	1.94±0.09			20.3	N	Y
Serpens	J182957.6+011304	18:29:57.66	01:13:04.60	-0.04	11.64±1.63	5.74±1.70	7.45±0.13	2.13±0.16	9.52±0.26	2.16±0.44	17.6		Y
Serpens	J182957.7+011405	18:29:57.73	01:14:05.78	-0.08	11.42±0.28		7.69±0.02	1.90±0.06			19.9	Y	Y
Serpens	J182959.0+011225	18:29:59.03	01:12:25.14	0.05	8.56±0.28		7.76±0.03	2.23±0.10			17.7		Y
Serpens	J183000.3+010944	18:30:00.30	01:09:44.71	-0.42	2.02±0.17		8.08±0.06	1.40±0.13			13.6	N	Y
Serpens	J183002.7+011228	18:30:02.73	01:12:28.22	0.18	4.02±0.20		7.60±0.04	1.64±0.10			16.8	N	Y
Serpens	J183005.2+004104	18:30:05.26	00:41:04.58	1.07	0.27±0.06		9.54±0.03	0.30±0.12			11.3	N	N
Serpens	J183005.7+003931	18:30:05.70	00:39:31.80	-1.18	0.84±0.09		9.77±0.02	0.46±0.05			11.3	N	Y

Note. — Columns are : (1) Cloud Name; (2) Source Name; (3) HCO⁺observed source Right Ascension in J2000 coordinates; (4) HCO⁺observed source Declination in J2000 coordinates; (5) Extinction corrected spectral index; (6) Integrated main beam HCO⁺line intensity, upper limits are computed as $\int T_{MB} dV + 2 \times$ the uncertainty in $\int T_{MB} dV$; (7) Integrated main beam HCO⁺line intensity if the source has double peaked emission; (8) Central line velocity at source position; (9) Width of line; (10) Central line velocity measured if the source has double peaked emission; (11) Width of line if the source has double peaked emission; (12) Extinction (A_V) measured at source position; (13) Flag indicating that the protostar does (Y) or does not (N) have at least one observed photometry point in the far-infrared or submillimeter ($70\mu m < \lambda < 850\mu m$). (14) Flag indicating that the protostar meets (Y) or does not meet (N) the HCO⁺line emission criteria to be categorized as a physical Stage 0+1 protostar. *A value of -999 for $\alpha_{E.C.}$ indicates the YSO is a known Class I source but does not have enough IR photometric points to calculate the spectral index.